Search for Higgs boson pair production in the $WWb\bar{b}$ final state at $\sqrt{s} = 13$ TeV with the ATLAS detector

Muhammad Sohail

Tutor : Biagio Di Micco
PhD Coordinator : Giuseppe Degrassi

A thesis submitted for the degree of Doctor of Philosophy (PhD) in Physics

September 2019

Acknowledgement

During PhD there are several people that I would like to thank for their support, collaboration and encouragement, resulting the completion of thesis. First of all I would like to thank to Istituto Nazionale di Fisica Nucleare (INFN) for supporting me financially for three years as well as for traveling to CERN.

First, I would like to give a big thank you to my advisors, Biagio Di Micco and Fabrizio Petrucci. Fabrizio Petrucci is the one who taught me things from scratch. Biagio put huge efforts to help me to improve the quality of thesis, which I am really appreciated. He helped a lot on both academic work and real life issue.

Working on ATLAS detector is not easy job. A new member working on the detector is just like a new swimmer struggling in the sea. But, I am lucky enough to have some nice guys supporting me when I am drowning. Marco sessa is the guy who motivated to join ATLAS experiment. He never refused when I asked him while stucked in coding. It was indeed a great honor to learn thing from him in a very easy way.

Finally, my deepest appreciation belongs to my family, especially to my parents and belowed wife who supported and encouraged alot in such a tense time.

LIST OF FIGURES

LIST OF TABLES

CONTENTS

CHAPTER 1

The Standard Model

The theory so called Standard Model was developed in the second half of the twentienth century to describe the observed phenomena in particle physics. The SM last particle still to be observed was discovered in 2012, that the Higgs boson. The Higgs boson is responsible to give mass to all SM particles. The theoretical context of the present thesis work is outlined in this chapter. The description described in this chapter is our current understanding, with a focus on the electroweak sector and the Higgs mechanism. This chapter also includes possible extensions to the SM Higgs sector that might be able to solve some of the shortcomings the Standard Model still faces today.

1.1 A General Overview

The Standrad Model (SM) of particle physics is a relativistic quantum field theory that describes the fundamental particles of matter and their interactions via the electromagnetic, weak and strong nuclear forces has been developed in the early 1970's. The SM has been verified several times by many high energy physics experiments and it explains successfully a wide variety of phenomena. The first step towards the formalization of the SM were taken by Glashow [1] Weinberg [2] and Salam [3] that describe the unification of the basic forces: weak, nuclear and electromagnetic. According to the SM matter is composed of basic building blocks known as quarks and leptons, that are point-like particles, having no internal structure and bosons that mediate the force careers among them. Charged leptons posses electric and weak charge while neutral leptons, i.e neutrinos, posses weak charge only. Figure 1.1 shows the schematic representation of the SM particles and their allowed interaction among them. The SM is mainly divided into two groups, i.e fermions and

bosons, a third category of particles is represented by the Higgs boson. It has spin-0 and is the only scalar particle ever discovered. The particles having integer spin called bosons (i.e gamma, photon etc) and those particles having half integer spin called fermions. Fermions obey the Fermi-Derac statistics while bosons obey the Bose-Einstein statistics. Fermions are catagorized into quarks leptons, which are then further divided into three generations (I, II and III) organized according to their properties as shown in figure 1.1; which summarizes the SM particles as well as their intrinsic properties i.e charge, spin, mass and electric charge while more detailed description of elementry particles is shown in table 1.1. The charge of the electromagnetic force is the electric charge and the mediating boson is the massless photon (gamma), the strong force takes place by the exchange of massless gluon (g) between the color charge particles and the weak force is mediated by exchanging the W and Z bosons for particles possessing weak charge. Quraks are considered charged under the electromagnetic, strong nuclear and weak force while fermions interact via the strong froce. Charged leptons possess electric charge as well as weak charge while neutral leptons possesses only a weak charge.

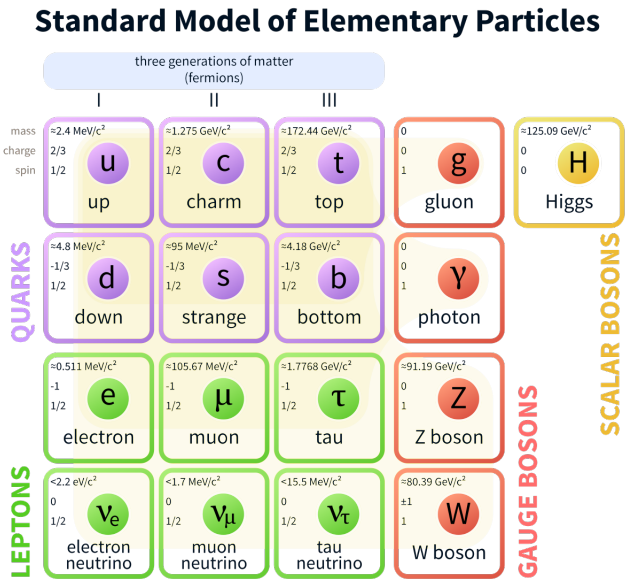

Figure 1.1: The constituents of the Standard Model and their masses, electrical charge and spin.

Table 1.1: Table shows the intrinsic properties of all SM leptons i.e mass, charge and life time [4].

Lepton	Charge	Mass	Mean Life
e	-1	0.510998928 ± 0.000000011 MeV	$> 4.6\text{x}10^{-6}$s
μ	-1	105.6583715 ± 0.0000035 MeV	$(2.1969811 \pm 0.0000022)\text{x}10^{-6}$s
τ	-1	1776.82 ± 0.16 MeV	(290.6 ± 1.0) x 10^{15}s
ν_e	0	< 225 eV(95%CL)	> 15.4 x mass s (90%CL)
ν_μ	0	< 0.19 MeV(90%CL)	> 15.4 x mass s (90%CL)
ν_τ	0	< 18.2 M eV(95%CL)	> 15.4 x mass s (90%CL)

The SM is a non-Abelian Gauge theory based on the symmetry group

$$SU(3)_C \otimes SU(2)_L \otimes SU(1)_Y$$

Where

- $SU(3)_C$ is the color symmetry group related to the strong interactions
- $SU(2)_L$ is the weak symmetry group of iso-spin related to the weak interactions
- $SU(1)_Y$ is the weak symmetry group of hypercharge related to the electromagnetic interactions

The full SM langrangian can be expressed as the sum

$$\mathcal{L} = \mathcal{L}_{gauge} + \mathcal{L}_{fermion} + \mathcal{L}_{\phi} + \mathcal{L}_{Yukawa} \tag{1.1}$$

1.2 Electroweak Theory

The Electrweak theory is the Uninamious description of the two of the four basic forces in nature: weak and electromagnetic force. This theory was proposed by Sheldon Glashow, Abdus Salam and Steven Weinberg during the 1960's. For this big contribution they were awarded nobel prize in 1979. More specifically the unification is based on the $SU(2)_L \otimes SU(1)_Y$ group, where L refers to left-handed particles while Y is the weak hypercharge the corresponding gauge bosons are the $W^{\pm}$ and Z^0, all of which are massless. In the SM, the $W^{\pm}$, Z^0 and photon are produced by the spontaneous symmetry breaking, caused by the electroweak symmetry caused by the Higgs mechanism briefly explained in 1.3. Because of this spontaneous symmetry breaking, the W_3 and b bosons coalesce into two different bosons i.e photon and Z^0 boson.

The Lagrangian of the electroweak interaction can be split in to four parts:

$$\mathcal{L}_{EW} = \mathcal{L}_{gauge} + \mathcal{L}_{Higgs} + \mathcal{L}_{f} + \mathcal{L}_{Yukawa} \tag{1.2}$$

In the above equation the first term is the gauge boson fields and can be expressed as

$$\mathcal{L}_{gauge} = -\frac{1}{4}W^a_{\mu v}W^{\mu v}_a - \frac{1}{4}B_{\mu v}B^{\mu v} \tag{1.3}$$

where $W^a_{\mu v}$ and $B_{\mu v}B^{\mu v}$ are the field strength tensors for the weak isospin and weak hypercharge respectively. The physical weak boson fields $W^{\pm}_{\mu}$, Z_{μ} and A_{μ} are the linear combinations of the W^a_{μ} and B_{μ} gauge fields and can be written as:

$$W^{\pm}_{\mu} = \frac{1}{\sqrt{2}(W^1_{\mu} \pm iW^2_{\mu})}, \tag{1.4}$$

$$Z_{\mu} = W^3_{\mu}cos\theta W - B_{\mu}sin\theta w \tag{1.5}$$

and finally photon field is

$$A_{\mu} = W^3_{\mu}sin\theta w + B_{\mu}cos\theta w \tag{1.6}$$

where θw called the Weinberg angle and can be expressed as

$$sin\theta w = \frac{gy}{\sqrt{g^2_w + g^2_y}} \tag{1.7}$$

and g_y is the coupling constant and the rest of the two lagrangian terms i.e $\mathcal{L}_{Yukawa}$ and $\mathcal{L}_{Higgs}$ are the only to give mass to the weak boson and fermions, are discussed in the next section.

1.3 The Higgs Mechanism

The $SU(2)_L \otimes U(1)_Y$ gauge symmetry needs to be spontaneously broken in order to give masses to the weak bosons i.e W and Z. This mechanism was jointly developed by three groups indepnedetly in 1964. They are Francios Englert and Robert Brout [10] Gerald Guralnik, Carl Richard hagen and Tom Kibble [11] and Peter Higgs[12]. The mechanism is labeled as the Higgs Mechanism.

$SU(2)_L$ doublet of complex scalar field can be written as :

$$\Phi = \begin{pmatrix} \phi_+ \\ \phi_- \end{pmatrix} = \frac{1}{2}\begin{pmatrix} \phi_1 + i\phi_2 \\ \phi_3 - i\phi_4 \end{pmatrix} \tag{1.8}$$

The lagrangian of this scala doublet is

$$\mathcal{L}_{Higgs} = (\partial^{\mu}\Phi)^{\dagger}(D_{\mu}\Phi) - V(\Phi) \tag{1.9}$$

and the potential can be defined as

$$V(\Phi) = \frac{\rho^2}{2}\Phi^*\Phi + \frac{\lambda^2}{4}(\Phi^*\Phi)^2 \tag{1.10}$$

having $\mu^2<0$ and $\mu>0$ corresponding to the potential with a Mexian hat shown in 1.3.

In general the minimum of the potential is chosen to be along the real part lower component of Φ as :

$$\Phi = \frac{1}{\sqrt{2}}\begin{pmatrix}0\\v\end{pmatrix} \tag{1.11}$$

to ensure that the photon remains massless. By chosing this minimum the symmetry is spontaneosly broken. The scalar field around the vacume expectation value in the unitary guage is expressed as :

$$\Phi = \frac{1}{\sqrt{2}}\begin{pmatrix}0\\v+h\end{pmatrix} \tag{1.12}$$

The Lagrangian can be expressed near this minimum and after expressing the first term one can obtains

$$(D^\mu\Phi)^\dagger(D_\mu\Phi) = \frac{1}{2}\partial_\mu h\partial^\mu h + \frac{(v+h)^2}{8}(2g_w^2W_\mu^-W_\mu^{+\mu} + (g_w^2+g_y^2)Z_\mu Z^\mu) \tag{1.13}$$

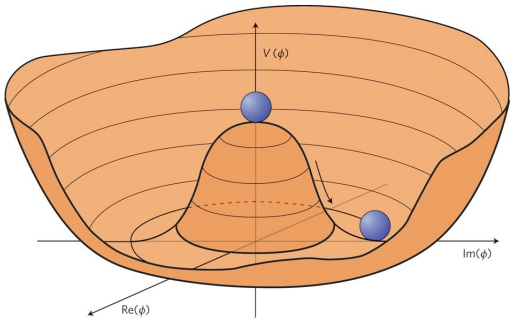

Figure 1.2: Graphical representation of Higgs potential for $\mu^2 < 0$.

From the above equation masses of W and Z bosons are identified as

$$m_w^\pm = \frac{vgw}{2} \tag{1.14}$$

$$m_z = \frac{vgw}{2cos\theta_w} \tag{1.15}$$

Using the muon lifetime the vacume expectatin value can be obtained as

$$v = \frac{2mw}{gw} = \frac{1}{\sqrt{\sqrt{2}G_F}} = 246GeV \tag{1.16}$$

G_F represents the Fermi coupling constant.

Now the Langrangian can be expressed by putting their values as

$$\mathcal{L}_{Higgs} = \frac{1}{2}\partial_\mu h \partial^\mu h + \frac{(v+h)^2}{8}(2g_w^2 W_\mu^- W_\mu^{+\mu} + (g_w^2 + g_y^2)Z_\mu Z^\mu) + \frac{\mu^4}{4\lambda} + \mu^2 h^2 + \lambda v h^3 + \frac{\lambda h^4}{4} \tag{1.17}$$

From this equation one can say that the coupling of vector boson is proportional to the square of the boson mass. Once the symmetry is broken, three out of four degrees of freedom in the Higgs field are absorbed to give the $W^\pm$ and Z boson their longitudinal components and remaining becoms the Higgs boson; a new scalar particle.

1.3.1 Single Higgs Boson Production

Decades after the Higgs theory was established, the Higgs boson was discovered on July 4^{th}, 2012 by the ATLAS and CMS collaborations [13]. According to the SM Higgs bosons are produced in different ways, although the probability of producing the Higgs boson in any collision is always extremely small because of its short life time i.e 10^{-22} sec. Only one Higgs boson is produced per 10 billion collisions at CERN. The most dominant Higgs boson production processes are explained below and their feynman diagrams are summarzed in figure 1.4.

Gluon-Gluon Fusion (ggF): It is the dominant Higgs boson production process at the Largr Hadron Collider(LHC). Two gluons from different colliding protons combine to form a loop of virtual quarks. On the experimental side, the ggF process has the largest cross section. And on the theoretical side, it is the most challenging process because of computing the top-loop. At $\sqrt{s} = 13$ TeV the cross-section of ggF is 43.93 pb^{-1} at LHC.

Vector Boson Fusion (VBF): After ggF, VBF is the second most important Higgs boson production mode at the LHC and has a cross-section 10 times less than ggF. In this process a quark and anti-quark pair scatter off each other via the exchange of W or Z bosons, the resulting vector boson fuses to produce a Higgs boson. The cross-section for the Higgs boson production through VBF

with a mass of 125 GeV at 13 TeV is 3.75 pb^{-1}.

Vector Boson Associated Production (VH): In this process a heavy vector boson is produced via quark or anti-quark annihilation and radiates the Higgs boson before decaying to any quark or lepton. The cross-section for the Higgs mass of 125 GeV at the LHC is 2.25 pb^{-1} at $\sqrt{s} = 13$ TeV. This process is also called Higgs Strahlung.

$t\bar{t}$ Associated Production (ttH): By this process the Higgs boson can be produced by fusing two gluons into a single gluon which then splits in to two top quark/anti-quark pair of which one top radiates a Higgs boson. The cross-section for the Higgs mass of 125 GeV at the LHC at $\sqrt{s} = 13$ TeV is 0.51 pb^{-1}. This is the least probable process of all processes at the LHC.

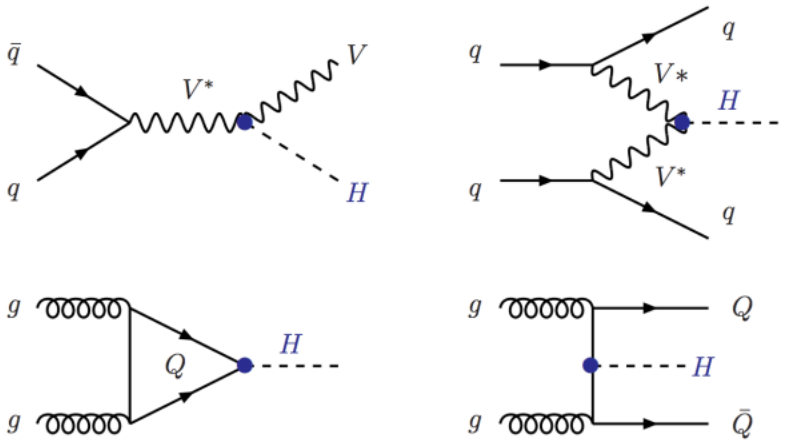

Figure 1.3: Feynman diagrams of the SM single Higgs boson production mechanisms in the hadron hadron collision at the LHC: associated production with vector boson (top left), vector boson fusion (top right), gluon gluon fusion (bottom left), associated production with heavy quarks (Q) where Q and $\bar{Q}$ show heavy quarks i.e top (bottom left).

The production cross-section of the SM Higgs boson with a mass of 125 GeV at the center-of-mass energies of 8 and 13 TeV are listed in Table 1.2.

1.3.2 Single Higgs Boson Decay

Once the Higgs boson is produced, it decays into a pair of particle and anti−particle in a very short interval of time i.e 10^{-22}sec. Coupling of the Higgs boson is proportional to the fermion mass and it is proportional to the boson mass squared: i.e the larger the branching ratio of the Higgs boson, the

Table 1.2: The SM Higgs production cross-section at $\sqrt{s} = 8$ and $\sqrt{s} = 13$ with $m_H = 125$ GeV as given in the Handbook of the LHC Higgs cross-section 4 [5].

Production Mode	σ_{8TeV} **[pb]**	σ_{13TeV} **[pb]**
Gluon-gluon fusion	21.42	48.58
Vector boson fusion	1.601	3.782
WH	0.7026	1.373
ZH	0.4208	0.8839
$t\bar{t}$H	0.1330	0.5071

larger the particle's mass coupled to the Higgs as shown in figure 1.4 and table 1.3 which explains that the bb and WW has the largest branching ration among all the possible decay channels. The $\gamma\gamma$ and the ZZ decay modes have larger signal to background ratio in comparison with the larger branching fraction decay mode.

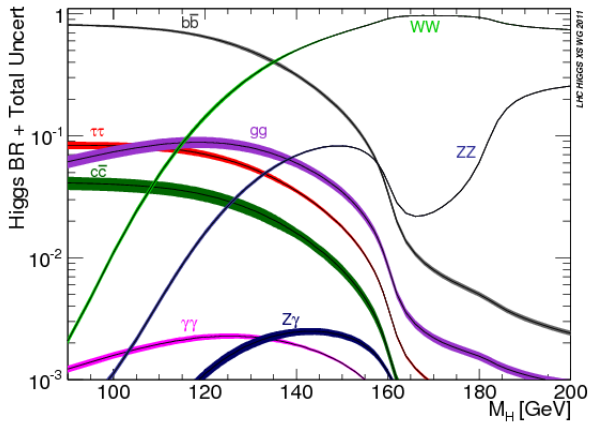

Figure 1.4: The different colored lines shows the standard model Higgs branching ratio across the range of 50 to 200 GeV. The vertical line at 125 GeV shows the Higgs boson branching ratios measured by ATLAS and CMS.

1.3.3 Double Higgs Boson Production

Just like single higgs boson production, diHiggs boson can also be produced in a number of ways i.e double higgstrahlung or higgs self-interactions. Searching for the diHiggs boson production through self-interaction will explore a new branch of high energy physics and it will have larger potential

Table 1.3: Higgs boson dominant branching ratios of a 125 GeV [6].

Decay Channel	BR [m_H=125 GeV]
Beam Energy (TeV)	7
H→bb	$(5.82\pm0.07)\times10^{-1}$
H→W^+W^-	$(2.14\pm0.03)\times10^{-1}$
H→gg	$(8.19\pm0.42)\times10^{-2}$
H→$\tau^+\tau^-$	$(6.27\pm0.10)\times10^{-2}$
H→cc	$(2.89\pm0.16)\times10^{-2}$
H→ZZ	$(2.62\pm0.04)\times10^{-2}$
H→$\gamma\gamma$	$(2.27\pm0.05)\times10^{-3}$
H→Z_γ	$(1.53\pm0.09)\times10^{-3}$
H→$\mu\mu$	$(2.18\pm0.04)\times10^{-6}$

for precesion Higgs boson measurement. The potential of the lagrangian can be written as:

$$\mathcal{L}_\phi = \frac{1}{2}(\partial_\mu\eta)(\partial^\mu\eta) - \mu^2\eta^2 \pm \mu\lambda\eta^3 - \frac{1}{4}\lambda^2\eta^4 + \frac{1}{4}(\eta^2/\lambda)^2 \tag{1.18}$$

The first two terms are the kinetic and mass terms and additional two terms addeded are proportional to η^3 and η^4 which represents the Higgs boson self-coupling. The several SM extensions require an enlarged higgs sector which contain many neutral higgs states. Currently the pressing task of the LHC is to search for an additional higgs boson having mass larger then twice of the single SM higgs boson and this can be produced through the Higgs self-interaction to which thesis is potentially sensitive. Feynman leading diagrams of the Higgs self-coupling and the Higgs-fermino Yukawa interaction is shown in 1.6.

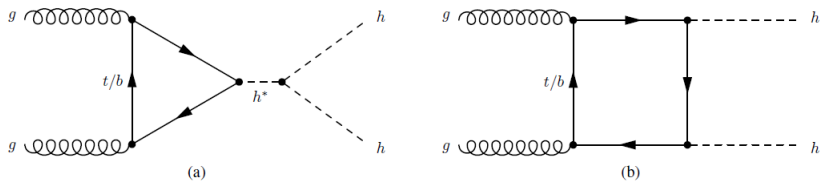

Figure 1.5: Non-resonant Higgs boson production.

According to the MSSM, five Higgs bosons are defined. One of them is the heavy neutral CP even Higgs boson denoted by H and can decay into pair of hh. Measuring rate of this CP even Higgs boson can be used to constrain the range of possible masses. Figure 1.7 shows the leading Feyman diagram of non-resonant Higgs boson decays to two Higgs boson to which this thesis is potentially sensitive.

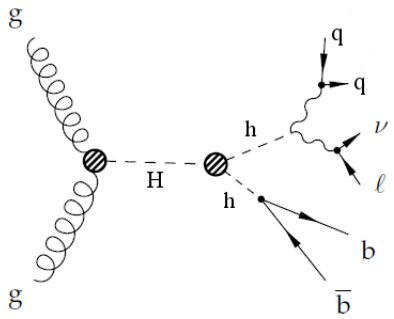

Figure 1.6: Resonant higgs boson production.

1.4 Higgs Boson Discovery

Searching for more than two decades, the two general purpose experiments i.e the ATLAS and CMS announced simultaneously the discovery of the Higgs boson on 4^{th} July 2012 at $\sqrt{s}$=8 TeV. The dataset used for this discovery was correspond to an integrated luminosity of 4.8 fb^{-1}. Five channels, $H \rightarrow ZZ^*$, $H \rightarrow \gamma\gamma$, $H \rightarrow WW^*$, $H \rightarrow \tau\tau$ and $H \rightarrow b\bar{b}$ were investigated for search of the higgs boson by the ATLAS experiment and was observed with a significance of 5.9 standard deviation and consistant with the SM Higgs boson as shown in figure 1.8; is the distribution of four lepton invariant mass while figure 1.10 is the diphoton invariant mass distribution observed by the CMS. A small peak in the around 125 GeV is the clear evidance of the higgs boson decays to diphotons. This channel is called golden channel having high signal-to-background ratio.

The CMS experiment data samples which was corredpond to an integrated luminosity of $5.3fb^{-1}$ at $\sqrt{s}$=8 TeV and CMS observed a significance of 5 standard devistion. Figure 1.9 shows the distribution of diphoton invariant mass while figure 1.11 shows the cross-section times branching fraction for ggF, VBF, VH and $t\bar{t}$ production for the respective decay modes. .

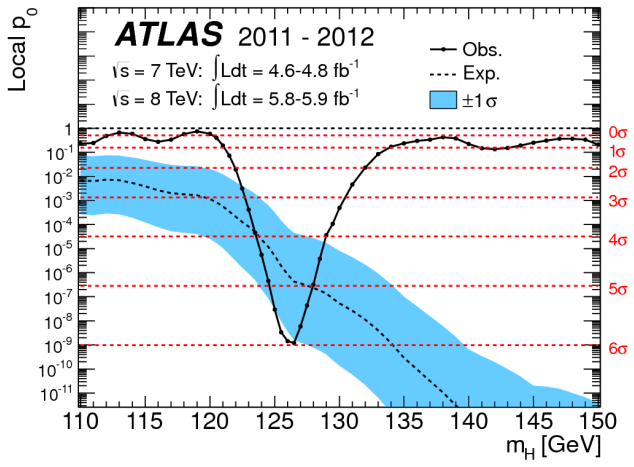

Figure 1.7: Local p-vlaue observed by ATLAS as a function of m_H.

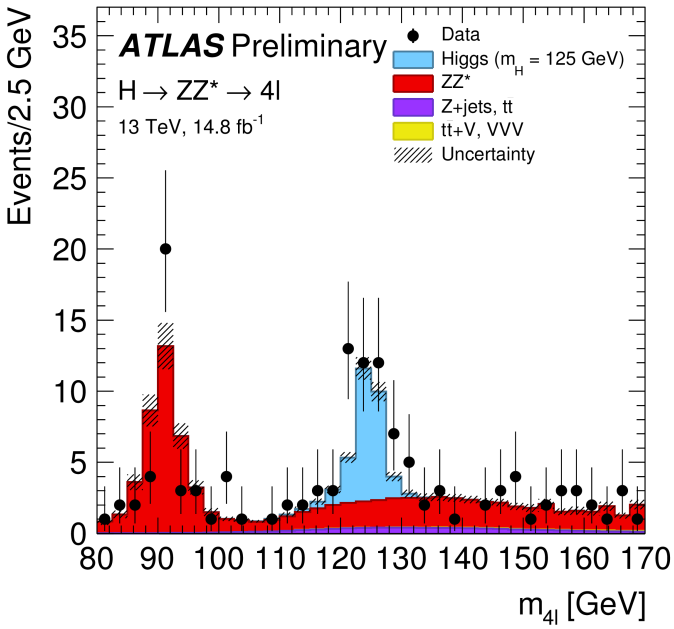

Figure 1.8: The histogram shows the discovery of Higgs boson. This is the invariant mass of four lepton. A small peak at 125 GeV shows the Higgs boson maass [7].

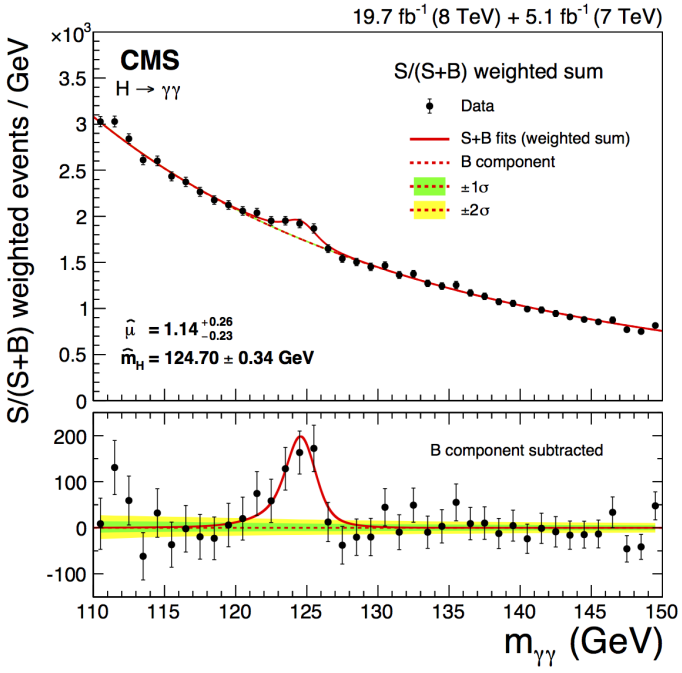

Figure 1.9: Diphoton invariant mass distribution observed by CMS. The lines represents the fitted signal and background while the color bands represents the standard deviation uncertainties [8]

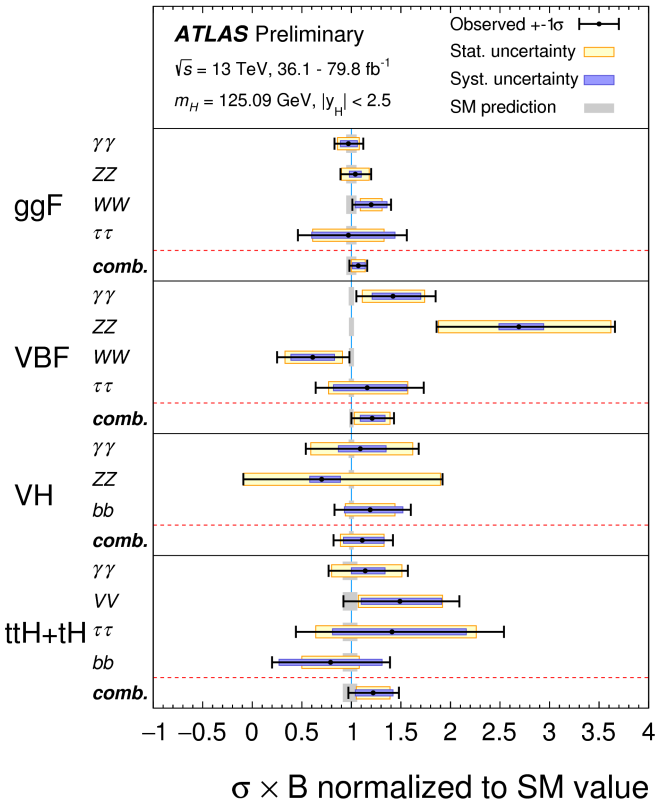

Figure 1.10: Figure shows the cross-section times branching fraction for ggF, VBF, VH and $t\bar{t}$ production in each relevant decay modes normalized to their Standard Model predictions [9].

1.5 Is Standard Model Complete?

The most important missing piece of the SM is the Higgs boson was discovered in 2012 at CERN after fouthy years of jounrney as discussed in [10] in more detail. It was the only missing piece? Is the SM now complete?

The SM is incredibly successfull and it is compatible with all experimental results. Despite of its success, there are still some issues which are listed below:

1. What is dark energy and is made of what?
2. What is dark matter? It is composed of some other type of particles? What are the principles which determined the available density of dark matter in our Universe? Are the sub particles of the dark matter interact with the SM particles?
3. How the Universe looked like at the inital stages just after Bing Bang? How it came to the current stage as we see today?
4. Are there any other forces which haven't observed yet? Are the known basic forces unified at very short distance as predicted by Weinberg, Glashow and Salam? Which mechanism the unification will follow?
5. Are the neutrino majorana? Why they are so light than other elememtry particles?
6. Why is there CP violation in quarks mixing? What mechanism finds the masses and mixing of quarks and leptons? Leptons violate CP?
7. The Higgs boson is an elementry or composite particle? The Higgs boson is the only one or so many? What are the principles that determines its coupling to leptons and quarks?

CHAPTER 2

The LHC and the ATLAS Detector

This chapter briefly describes the apparatus used to perform measurements in the context of the SM and beyond as described in chapter 1. The LHC, is the largest circulator accelerator at CERN ever built to test the SM, exotic theories and other rare processes very precisely. At the moment four main experiments are operational, recording data of proton-proton (pp), proton-lead ($p-pb$) and lead-lead ($Pb-Pb$) collision with the center-of-mass (CM) energy at 14 TeV. Two of them are the general purpose eperiments: A Toroidal LHC ApparatuS (ATLAS) and Compact Muon Soleniod (CMS). Large Hadron Collider beauty (LHCb) and A Large Ion Collider Experiment (ALICE) are focused in search of b-Physics beyong the SM and Quark Gluon Plasma (QGP) respectively.

2.1 The LHC Performance and Beam Structure

The LHC is a superconducting collider and the particle accelerator based at CERN which is situated on the border of Switzerland and France near the city of Geneva. The accelerator has a circumference of 27 Km and it lies in the tunel of 100 meter undergroud, which makes it the largest ever built man made machine in the history of Universe. The maximum number of bunches possible in the LHC is 2802 [14]. Group of bunches are called bunch trains. The distance between the bunches was 50ns in Run1 and in Run2 it is reduced to 25ns. To reach the desired luminosity and CM energy the only the LHC accelerator is not enough but it has a chain of injectors. Before bunches of proton beam are delivered to the HLC by a complex of accelerators of different circumferences consists of Linear Accelerator 2 (Linac2; started in 1978 and replaced the Linac1), the Protron Synchrotron Booster (PSB), Proton Synchrotron (PS) and the Super Protron Synchrotron (SPS)

as shown in Fig 2.1. The Linac2 is the initial of the pp collision at CERN ind it uses radio frequency to charge the cylindrical conductors. The proton passes through the conductors either positively or negatively charged [15]. The conductors behind them push the particles and the conductors ahead of them pull, causing the particles to accelerate. The proton source is a bottle of hydrogen gas at one end of the Linac2. The hydrogen is passed through an electric field to strip out electrons, leaving only protons to enter the accelerator. In the Linac2, the particles gain an energy of 50 MeV and then the protrons are injected in to another circular accelerator, Protron Synchrotron Booster, made of four superimposed synchrotron ring where particles gains an energy of 1.4 GeV.

Protons are then injected in to the PS. It is the key component at CERN's accelerator complex and it accelerates proton delivered by PSB and beam energy rises to 26 GeV. Before entering the beam in to the LHC, the SPS is used to inject the beam to gain an energy of 450 GeV. SPS is a 7 Kilometer in circumference and the second largest accelerator mechine at CERN. The NA61, NA62, SHINE and the COMPASS experiments are installed in this accelerator. A major highlight came in 1983 with the Nobel-prize-winning discovery of W and Z particles, with the SPS running as a proton-antiproton collider [16]. The CERN accelerator complex showing the succession of accelerator machines. The four main experiments ATLAS, CMS, ALICE and LHCb are depicted in figure 2.1.

Inside the LHC accelerator two proton beams are traveling close to the speed of light before they get ready to collide. The two pp or $Pb-Pb$ beams travel in two separate beam pipes of 5cm each kept at ultrahigh vacuum. Beams are guided by the superconducting electromagnetics around the accelerator providing a strong magnetic field. These magnetis are built from the cables of special material operating at superconducting state. Beams are focused by using the quadropole magnetsa and the acceleration is done by the radio freuency (RF) cavities. 1232 superconducting magnets are installed at the LHC which provides proper magnetic field of 8.3 T. A few of the most important LHC parameters are listed in table 2.1. To achieve physics goals in collider, the instantaneous luminosity which is proportional to the production rate can be written as:

$$\frac{dN}{dt} = L * \sigma \tag{2.1}$$

Where sigma (σ) is the cross section of the process and L is the instantanous luminosity depends on the properties like time and number of bunches in the machine.

The luminosity is an important factor of an accelerator. It is the measurement of the number of collision take palce in a detector per cm^2 per second. The Luminosity and the number of collision

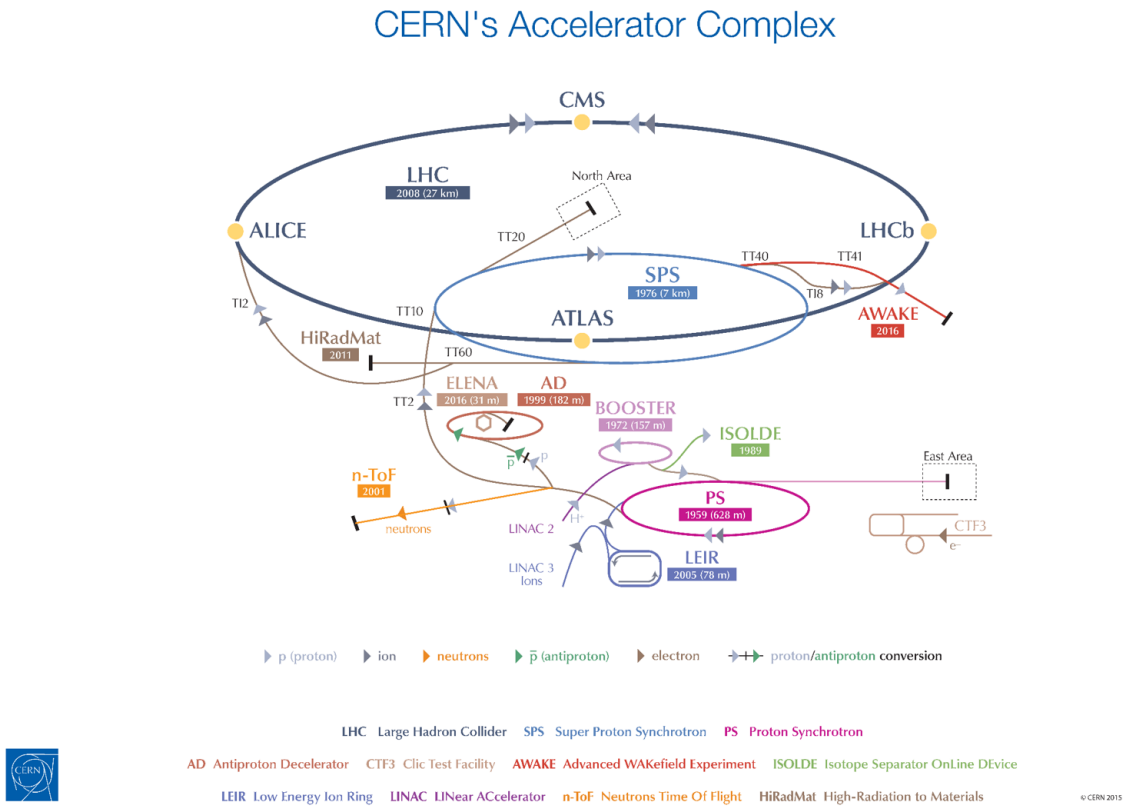

Figure 2.1: The CERN accelerator complex showing the succession of accelerator mechines. The four main experiments ATLAS, CMS, ALICE and LHCb are depicted [23].

are proportional to each other. The larger the L, the larger will be the number of collision and to calculate it we need to tabke into account the cross section. In figure 2.2 shows the cross sectional view of how the collision take place at the LHC. During Run1 in 2011 the LHC started to deliver pp collision at 7 TeV center of mass energy. During turn on in 2008, one of the links between superconducting magnets was failed, leading to an explosion that damaged several other magnetis [17]. During the LHC operation in 2010 and 2011, it was operated at 7 TeV. In 2012 this center of mass energy was increased to 8 TeV leading to collect an integrated luminosity of 21.7 fb^{-1}. The years 2014 and 2015 was dedicated to a long shutdown to modify a series of parts. In 2015 the LHC was put forward to collect new data and collected an integratrd luminosoty of 33.1 fb^{-1} in 2016. Integrated luminosities of Run2 and commulative luminosity versus day delivered to ATLAS during stable beams and for high energy pp collisions are shwon in figure 2.3.

Table 2.1: Comparison of LHC main parameters in 2011 and 2012[25].

Parameter	**2011**	**2012**	**Design**
Beam Energy (TeV)	3.5	4	7
Max Number Bunches Colliding	1854	1380	2808
Bunch Intensity	1.5	1.48	1.15
Bunch Spacing [ns]	50	50	25
Peak Inst. Luminosity	3.65	7.73	10
Avg. Inelastic Interactions per crossing	9.1	20.7	19
Peak Inelastic Interactions per crossing	34	72	
Trans. Norm. Emittance	1.9-2.3	2.6	3.75
Longitudinal Emittance			2.5
IP Beam Spot	25	19	16.7
Beam Current [A]	0.38	0.41	0.582
RMS Bunch Length [cm]		9	7.55
Crossing Angle	240	290	285

Table 2.2: LHC main parameters showing symbols, unit and value[25].

Parameter	**Symbol**	**Unit**	**Value**
Machine circumference	2πR	[m]	26658.883
Number of arc			8
Ring separation		[mm]	194
Number of insertion			8
Number of interaction point			4
Energy	E	[TeV]	7.0
Dipole field	B	[T]	8.4
Luminosity	L	$[cm^{-2}s^{-1}]$	10^{34}
Injection energy	E_i	[GeV]	450
Number of bunches	n_b		2835
Bunch spacing	τ_b	[ns]	24.95
Particle per bunch	N		1.05×10^{11}
Stored beam energy	E_s	[MJ]	334
Normalized transverse emittance	ϵ		3.75
β-value at IP	β^*	[m]	0.5
rms beam radius at IP	σ^*		16
γ transition	γ		53.7
Luminosity per bunch collision	L_b	$[4cm^{-2}]$	3.14×10^{26}
Crossing angle	ϕ		200
Revolution frequency	f_{rev}	[kHz]	11.1
Luminosity reduction factor	F	[rad]	0.9

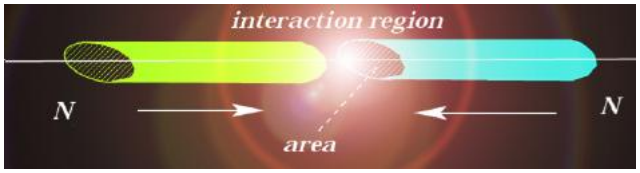

Figure 2.2: Cross sectional view of proton-proton collision [24].

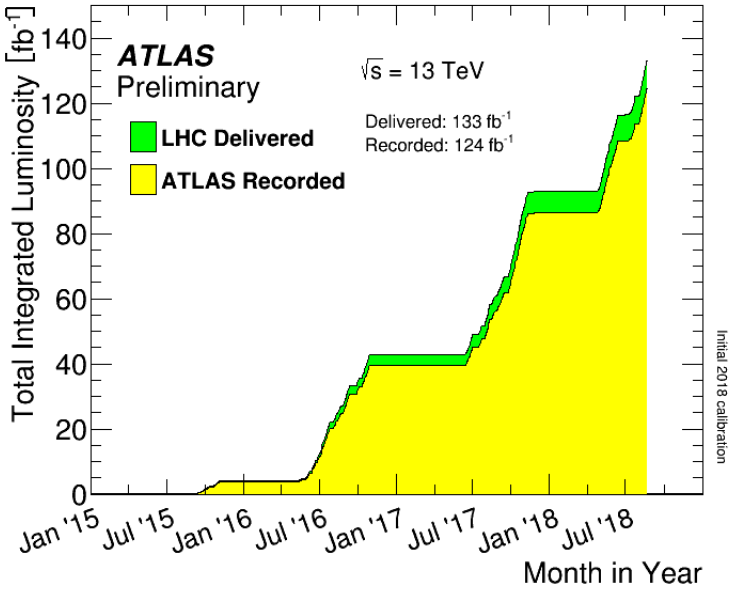

Figure 2.3: Figure shows the total integrated luminosity at run 2.

2.2 Upgrades to the High-Luminosity LHC

The High Luminosity Large Hadron Collider (HL−LHC) is a proposed upgrade to the LHC to be functional in 2025. One of the goal of the HL−LHC is to increase the luminosity of the meching by a factor of 10 and this will increase the chances to see the rare decay process i.e $hh \rightarrow WWb\bar{b}$ and so many others. After increasing the luminosity the LHC will be able to observe 15 million Higgs bosons every year and in Run1 only 1.2 million was obserbed. The phase-I of the LHC will take place in 2019-20 is called long shutdown-2 with the aim of reaching the 14 TeV center of mass energy and phase-II the so called 3rd long shutdown (2024-2026) with aim of increasing the integrated luminosity of 250 fb^{-1}. This HL-LHC will costs about 10 million CHF over a period of ten years. Figure 2.3 shows the HL-LHC plan for the comming two decades.

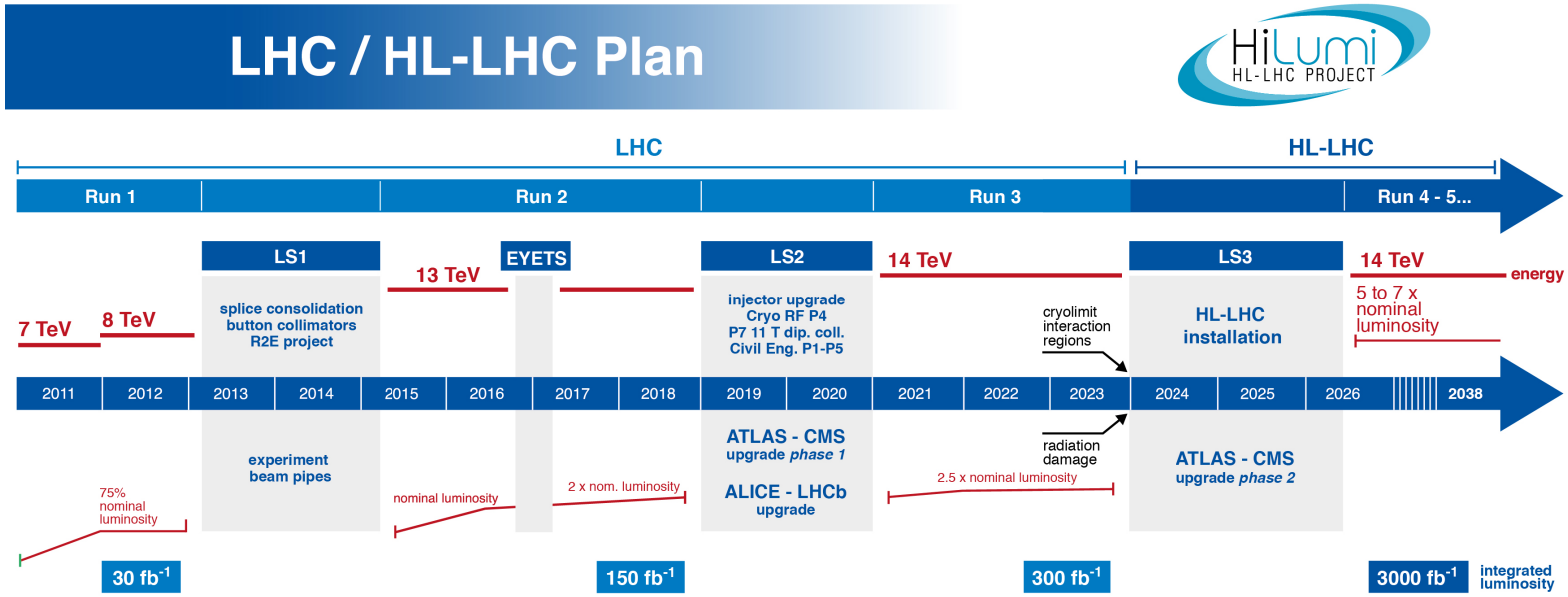

Figure 2.4: High Luminosity Large Hadron Collider plan for the comming two decades specifying different TeV scales, where luminosity will be reached upto $3000 fb^{-1}$ by the end of 2038.

2.3 The ATLAS Experiment

ATLAS is one of the main four large detectors installed at the LHC. It stands for A Toroidal Large hadron collider ApparatuS. It is a general purpose detector; it can search for different kind of Physics for example Higgs boson, extra dimensions, SUSY and Dark matter etc. It has a cylinderical shape having length 44m, height 22m and weights about 7000 tons. Due to the *pp* collision particles are produced at the interaction point of the ATLAS. It has a large collaboration including 3000 scientists from 200 Universities of 40 different countries. The LHC has 8 points (stations) and ATLAS is built on point one located in Switzerland.

ATLAS consists of several concentric sub detectros each of them is dedicated to special particle detection. The series of detectors are the Inner Detector (ID)[18][19]. It consists of Pixal Detector (PD), Transition Radiation Tracker (TRT) and Semicondtuctor Tracker (SCT). The ID is surrounded by the Calorimeters system, consists of liquid argon electromangeitc system, tile calorimeter, liquid argon hadronic end-cap calorimter and forward detector.

The last and outermost part of the ATLAS detectors is the Muon Spectrometer(SM) [20]. The MS consists of two end-caps and one barrel. It is designed to measure the muon trajectories. Each of these parts of ATLAS will be discussed in the following sections. A cut-way and cross-sectional views of the ATLAS is shown in figure 2.5.

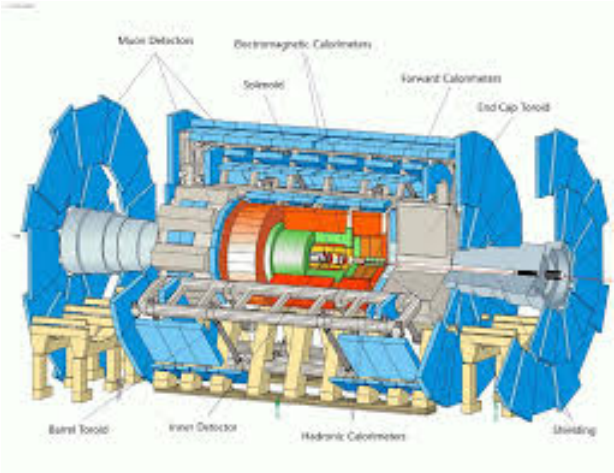

Figure 2.5: The cross sectional view of the ATLAS detector [24].

2.3.1 The Inner Detector

The basic function of Inner Detector (ID) (see Fig. 2.6) is to measure the momentum of charged particles and to reconstruct primary and secondary vertices. It is immersed in a 2T solenoidal magnetic field and is composed of three sub-detectors: the pixel and semicondtructor tracker (SCT) uses silicon planer technology while Transiation Radiation Tracker (TRT) employes a drift chamber using staw tubes filled with gas. Briefly subdetectors of inner detectors are described and a zoomed view of end-cap and barrel of the ATLAS inner detector is shown in figures 2.7 and 2.8.

Pixel Detector : The Pixel Detector [21] provides charged-particle tracking with very high efficiency over the pseudorapidity range $|\eta|<2.5$. It is the inner most part of the ID, using in reconstruction and identification of secondary vertices of different particles. It provides a pattern recognition capibility to meet the track reconstruction requirements of the ATLAS detector and it contains about 80 million channels. Every pixel sensor has a minimal R-ϕxZ pixel size of 50x400μm^2 and interinsic resolutions of 10μm in R-ϕ and 115μm in Z for both the barrel and endcaps.

Semiconductor Tracker : The SCT is composed of cylindrical layers in the barrel and nine disks at each endcap. The barrel consists of 2020 modules made of silicon strip sensors and the end-cap consists of 1976 wedge-shaped strips, the radii of the layers are about 30cm, 37.3cm, 44.7cm and 52cm the disks of the end-cap are placed in z-direction between 85cm and 272cm for each side [22]. Both the pixel and SCT provide an average eight high-precision hits per track.

Transition Radiation Tracker : The TRT is composed of nearly 300,000 drift tubes having diameter of 4mm. They have gold-plated tungsten wires at the center of 31μm diameter. Each tube is filled with gas mixture of 70% Xe, 27% CO_2 and 3% O_2 and acts as a propotional counter. The drift tubes are placed in the barrel parallel to the beam covering from 560 to 1080 mm in radius and $z<720$ mm. When a particle passes the TRT drift tubes ionizes the gas and produces 5 to 6 ionization clusters per mm in the gas. At last the signal produced in straws are amplified, shaped and then finally discriminated. At the start of the ATLAS operation the gas used in the TRT was xenon but due to large gas leaks the TRT is now flushed with gas composed of argon. TRT offers a good discrimination between electron and hadrons.

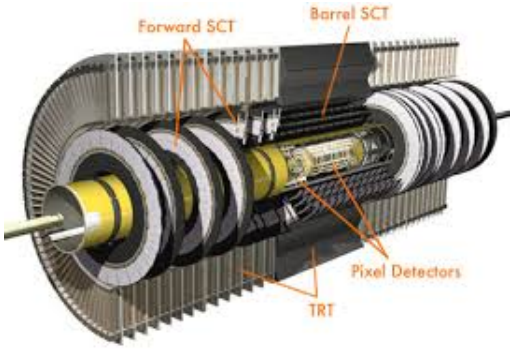

Figure 2.6: The ATLAS inner detector [24].

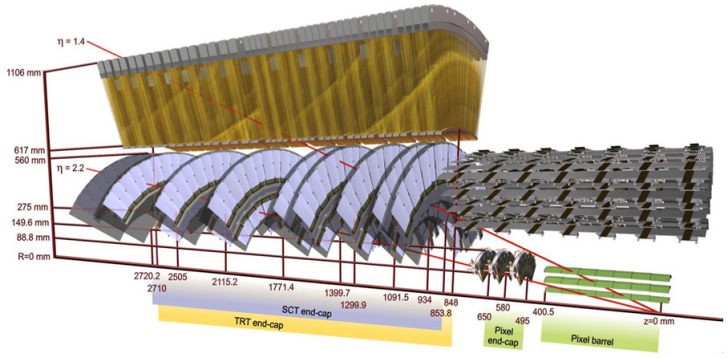

Figure 2.7: A zoomed view of end-cap of ATLAS inner detector[24].

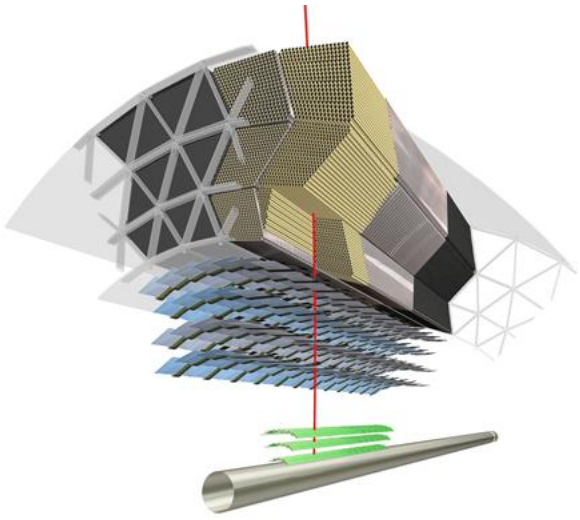

Figure 2.8: A zoomed view of barrel of ATLAS inner detector[24].

2.3.2 The Calorimeter System

The ATLAS calorimeter system (see figure 2.9) is used to measure the energy of electrons, photons, hadrons and jets as they pass the detector. Its basic function is to absorb all the particles coming from the collision point by forcing them to deposit all of their energy within the detector. Calorimeters usually consists of layers made of high density materials like lead. The ATLAS calorimetery system is composed of an electromagnetic (ECAL) and hadronic calorimeters (HCAL) covering rapidity region up to $|\eta|$<4.9. Am important parameters of the calorimeter system of the ATLAS detector is shown in table 2.3.

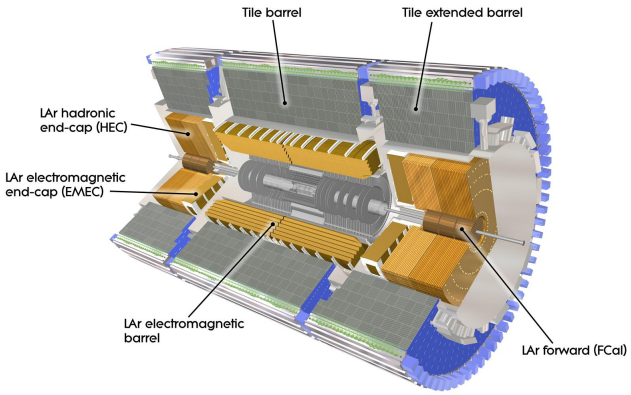

Figure 2.9: The ATLAS calorimeter system [24].

The Electromagnetic Calorimeter

The EM calorimeters are divided in barrel (EMB) and end-cap (EMEC). The EMB uses LAr as active material and lead as absorber and the full system covers a pseudorapidity of $|\eta| < 1.475$. The first layer has the best granularity in η while the second provides a better resolution in ϕ. The number of radiation lengths in the EMB is 24 X_0. The EMEC calorimeters are made with the same material of the EMB but the number of radiation lengths in the end-cap is larger (26 X0). In the end-cap the EM is composed of two concentric wheels covering the range 1.375 <$|\eta|$< 3.2.

The Hadronic Calorimeter

The hadronic calorimeter system is located after the EM calorimeters. As the EM, it is divided in a barrel (TileCal) and two end-caps (HEC). The TileCal is composed by steel, as absorber, and plastic scintillators, as active material. The number of interaction lengths in the TileCal is about 9 λ. The HEC is composed of LAr and copper and it covers up to $|\eta| < 3.2$. It is divided in two

wheels for each end-cap. In the end-cap regions the total number of interactions lengths (including the EMEC) is 12 λ. To cover pseudorapidity larger than $|\eta| > 3.2$ another calorimetric is used: the forward calorimeter (FCAL). FCAL is composed by one EM and two hadronic calorimeters and covers between $3.1 < |\eta| < 4.9$. The number of interaction lengths is about 10 λ.

Table 2.3: Important parameters of Calorimeter system of ATLAS .

	barrel	**end cap**
EMCal		
$\|\eta\|$ coverage		
Presampler	$\|\eta\|<1.52$	$1.5<\|\eta\|<1.8$
Calorimeter	$\|\eta\|<1.35$	$1.375<\|\eta\|<1.5$
	$1.35\|\eta\|<1.475$	$1.5<\|\eta\|<2.5$
		$2.5<\|\eta\|<3.2$
Number of readout channels		
Presampler	7808	1536 (both sides)
Calorimeter	101760	62202 (both sides)
LAr Hadronic end-cap		
$\|\eta\|$ coverage		$1.5 <\|\eta\|<3.2$
Layers		4
Readout		5632 (both sides)
LAr forward calorimeter		
$\|\eta\|$ coverage		$3.1 <\|\eta\|<4.6$
Layers		3
Readout		3524
Tile Calorimeter		
	barrel	Extended
$\|\eta\|$ coverage	$\|\eta\| < 1.0$	$0.8 <\|\eta\|< 1.7$
Layers	3	3
Readout	5760	4092 (both sides)

2.3.3 The Muon Spectrometer

The Muon Spectrometer (MS) [27] is the outer most part of the ATLAS detector and surrounds the calorimeter system. The function of the MS is to precisely measure the path produced by traversing muons, independently of the ID. The MS is placed at the very end as muons loses very small amount of energy during ionization (dE/dx) because of its high mass make it possible for it to pass all the subdetectors without producing any trajectory. There are four main technologies used in the MS all are gas filled detector operating as a proportional chambers. The MS needs a magnetic system in order to bend the muon trajectories to measure its momentum. Magnetic system is composed of barrel extending over a length of 25 meters and two end-caps are inserted in barrel at

each end covering a region of 1.6< $|\eta|$<2.7. Over 1.4 < $|\eta|$< 1.6 usually refered as a transition region, where magnetic deflection is provided by the combination of both the barrel and the end-caps.

The MS is consists of one barrel and two end-caps and both of them has three layers. Incase of barrel each layer is in a cylinderical shape with different radii at different points while end-cap is like a disk which is usually called a wheel. On the basis of the distance from the interaction point, the wheels are labeled as Inner, Middle and Outer wheels as depicted in figure 2.10.

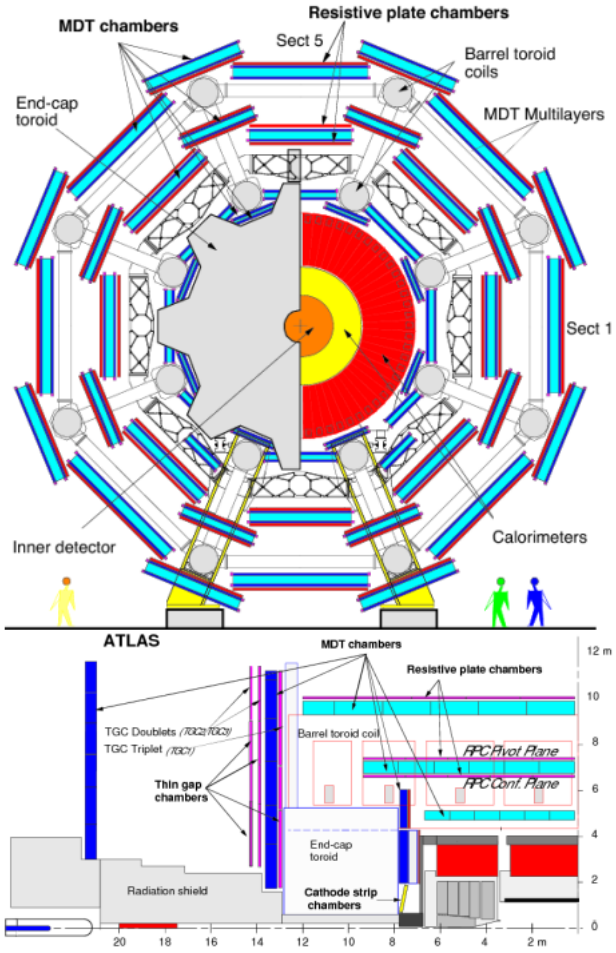

Figure 2.10: Geometric layout of muon sub-detectors in barrel (up) and end-cap (down) region [28].

Monitored Drift Tubes

The MDT's are deployed in barrel as well as in the end-cap regions. They are 1088 chambers in total and consists of two multilayers of MDT's, separated by a frame composed of three cross-plates and two long-beams (see figure 2.11). Each tube has a diameter of 3cm and 400μm thickness. A composition of two gases is used in MDT's i.e 93% Ar +7% CO2 operating at 3 bar pressure. The MDT chambers provides an angel and position of the charged particles passed in the local zt-plane, thus produces circles around anode wire called drift radius and has to be extraced from a drift time measured by the tube as shown in figure 2.12. To achive more better precision measurement than 10 percentage for a 1 TeV muon, the resolution of one MDT has to be less then 80 micro meter for which calibration is required.

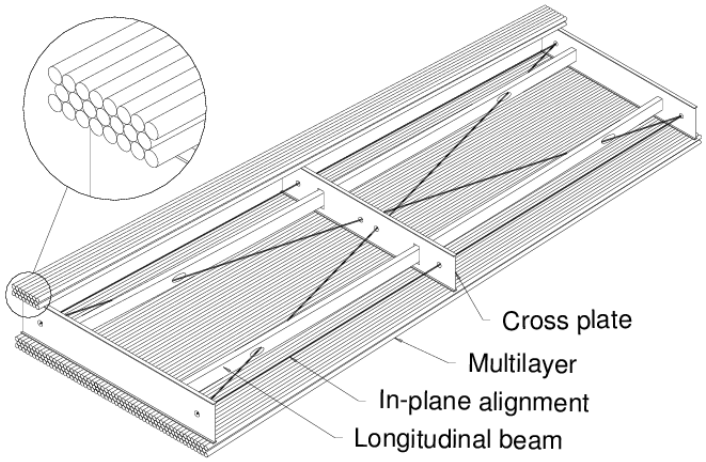

Figure 2.11: Scheme of a Monitored Drift Tube chamber [29].

Cathod Strip Chambers

The Cathod Strip Chambers (CSC's) [30] are multiwire proportional chambers using a gas mixture of Ar, CO2 and CF4. They have resolution time of about 7 nano sec and are deployed at large pseudorapidities ($2.0 < |\eta| < 2.7$) to reconstruct the muon tracks. The CSC's are divided into 16 sectors in total, 8 including small and 8 large wheels. They are used in the innermost tracking layers becuase of their time resolution and high capibility rate.

Resistive Plate Chambers

The Resistive Plate Chambers (RPC's) are used only in the barrel covering $|\eta|<1.05$. RPC's are composed of 544 chambers and deployed in three concentric circles alternatively to MDT's. They are wireless gacious parallel electrode-plate detectors [31]. Two RPC's are kept parrallel to one and

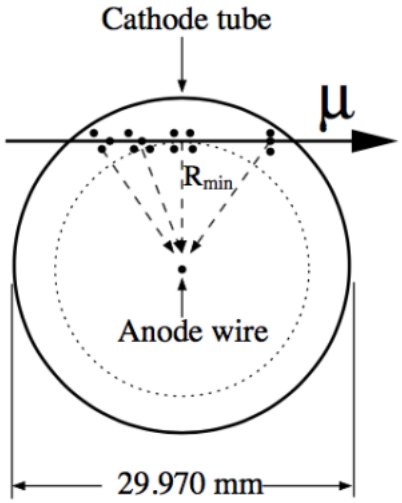

Figure 2.12: Interaction of a muon with the MDT gas produces primary electron along its way which drift towards the anode wire [29].

other having 3mm distance inbetween them.

Thin Gap Chambers

The Thin Gap Chambers [33] are multiwire proportional chambers having very small distance between the cathode and wire i.e 1.4 mm. The smaller distance between two wires is 1.8 mm. These properties leads to very good time resolution for trigger purposes. They are deployed in the end-cap region of the MS as shown in figure 2.10. They covers pseudorapidity ranging $1.5 < |\eta| < 2.7$.

Forward Detectors

In addition to the Calorimeter system and Muon spectrometer, ATLAS is equipped with the LUCID, ZDC and ALFA detectors having the ability to partially cover the forward rapidity region. The purpose of these detectors is to measure cross-section and luminosity. Main parameters of the ATLAS muon system is given in table 2.4.

Table 2.4: Main parameters of muon system [25].

Muon Drift Tubes	**MDT**
Coverage	$\|\eta\|<2.7$(innermost layer:$\|\eta\|2.0$)
Number of Chambers	1088
Number of Channels	339000
Function	Precision tracking
Cathode Strip Chambers	**CSC**
Coverage	$2.0<\|\eta\|<2.7$
Number of chambers	32
Number of chanlles	31000
Function	Precision tracking
Resistive Plate Chambers	**RPC**
Coverage	$\|\eta\|<1.05$
Number of Chambers	544
Number of Channels	359000
Function	Triggering, second coordinate
Thin Gap Chambers	**TGC**
Coverage	$1.05<\|\eta\|<2.7$
Number of Chambers	358
Number of Channels	318000
Function	Triggering, second coordinate

2.4 Magnetic System

An appropriate magnetic field distribution throuthout the detector is required to measure the transverse momentum of charged particles produced during pp collision. The ATLAS magnetic system consists of four different supermagnetic magnets:

- A central soleniod
- An air-core barrel toroid
- Two air-core end-cap toroids

The central soleniod consists of one coil with 1173 turns. It provides a magnetic field of 2 T for the inner detector. It is deployed in the barrel region and infront of the calorimeter system. The magnetic field points in the positive z-direction.

Each toroid magnet consists of eight coils with 120 and 116 turns in barrel and end-cap respectively. These coils are operating at temperature of 4.5 K and provides a magnetic field of about 0.5 T which allows the muons to bend. Figure 2.16 shows the sketich of the ATLAS magnetic system. A three dimentional sketch of the magnetic system of the ATLAS detector is shown in figure 1.13.

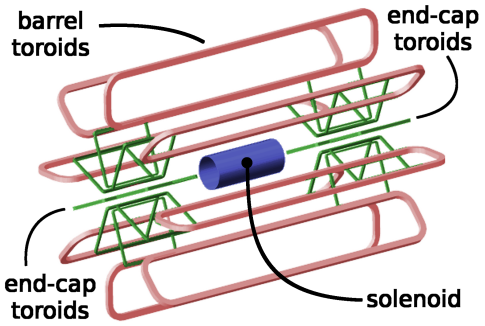

Figure 2.13: A three dimentional sketch of the magnetic system of the ATLAS detector.

CHAPTER 3

Hadron Collider Physics

In this chapter we will study the collider phenominology including the production of different particles, the final state and modelling of these processes at the LHC as a result of pp collisions. The proton is a hadron and it is composed of quarks and inbetween them only strong forces eixst. This is the reason that strong force plays a vital role in hadron collision.

The processes produced at any hadron collider can be factorized in the following stages:

1. Parton distribution function
2. Hard scattering of partons
3. Parton showser including initial and final state radiation
4. Hadronisation
5. Required event

All of the above mentioned processes will be explained in the following sections.

3.1 Parton Distribution Functions

Parton distribution functions are one of the main source of uncertainity in hadron colliders. Figure 3.1 shows the Feynman diagram of processes that take place in pp collision at the LHC. The protons coming are indicated by the parallel lines. Suppose the protons of momenta P_1 and P_2 having center-of-mass energy $s = (P_1 + P_2)^2$. The protons consist of several partons and the hard

scattering are the processes indicated by the box with cross section in figure 3.1. In the same figure the interacting partons carry momenta $x_1.p_1$ and $x_2.p_2$ and the partonic center-of-mass energy can be expressed as $s = sx_1.x_2$. The parton distribution function $f_a(x, Q^2)$ describes the probability that a parton carry momentum x while Q^2 represents the energy scale. Figure 3.2 shows the two PDF i.e $f_a(x, Q^2)$ and $g_a(x, Q^2)$ for general scenario and f and g are equally distributed at the LHC.

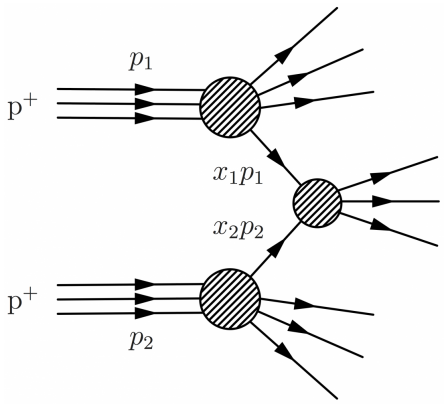

Figure 3.1: A Feynman diagram of proton-proton collision takes place at the LHC.

The QCD factorisation theorem allows for the separation of short and long distance physics, where the PDF includes the long distance processes and sigma contains the short distance processes such that the total cross section for a process $pp \rightarrow$X can be written as:

$$\sigma_{pp} \rightarrow X(x_1, x_2, Q^2, \sqrt(s)) = \sum_{a,b} \int dx_1 \int dx_2 f_a(x_1, Q^2) g_b(x_2, Q^2) \sigma_{ab \rightarrow X}(x_1, x_2, Q^2, \sqrt(s)) \quad (3.1)$$

The sum is for all partons coming form the hadron collisions. The parameters, i.e deep inelasctic scatternig [1], are measured in particle collision and the kinematic (rapidity [2]) distributions of $W^{\pm}$ and Z^0 in hadron collision can be used to meaure the PDFs. In figure 3.2 PDFs for the partons at a scale of $Q^2 = 100$ GeV are shown. The large momentum is carried out by the up and down quarks while for the lower x gluons dominates the parton content.

[1] The deep inelastic scattering is basically the collision of pasitrons and electron

[2] The rapidity is commonly used as a measure for relativistic velocity and mathematically can be written as $y = \frac{1}{2} \ln \frac{E+p_z}{E-P_z}$

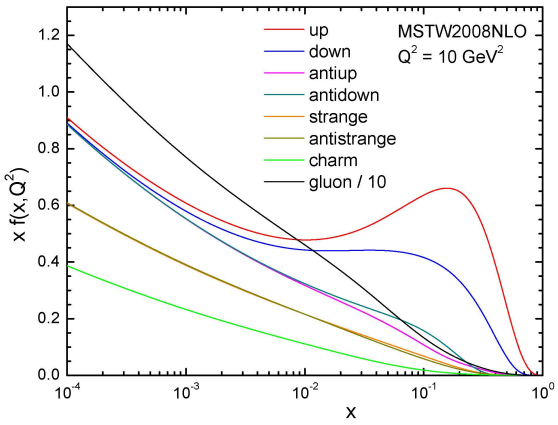

Figure 3.2: The CT10 parton distribution functions evaluated at a Q of 10 GeV.

3.2 Monte Carlo Simulation

The Monte Carlo (MC) is a broad class of computational algorithms used to simulate a complete any physics event occured in any collider behaves as a theory. This theory is then compared with the data taken for agreement/disagreement. In this section overview of important MC concepts for particle physics analysis are explained. The MC generators take random number as inputs, that is discussed in the next section, both used for the integration and event generation.

3.2.1 Monte Carlo Integration

One need integrals and can not be solved analytically while calculating measurable quantities i.e cross section or differential cross section. One of the best method is the MC integration techniques to use and it uses pseudo random numbers as an input, generated on the basis of a certain distribution.

3.2.2 Event Generation

After calculating integrals makes it easy and possible to generate the whole event occured. The MC generators are uses true random variables as an input and this make it possible the calculation of cross section of a specific interaction. Figure 3.3 shows a complete and complex collision process. The underlying event is represented by the purple color and it is the proton remnant interactions.

Quark and gluons are the inital and the final state radiations will develop parton showser shown in blue color and final state of this event is shown in green color, is the hadronization produced by the showered particles. The job of MC event generators is to simulate these processes in a probabilistic manner. There are several MC event generators used by the various particle physics experiments. Only three of them are used in this analysis i.e PYTHIA, POWHEG and SHERPA are briefly explained in the next sections.

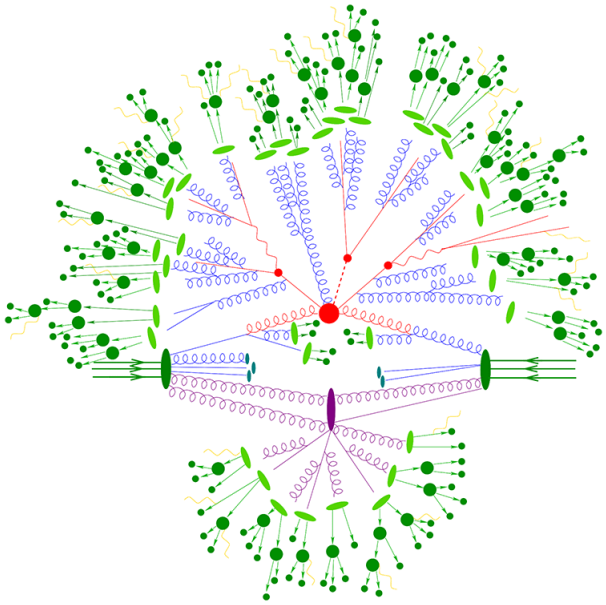

Figure 3.3: Schematic diagram of processes takes place in any event in hadron-hadron collision. The processes includes hard process, parton shower and hadronization. The different colors shows the various processes involved.

Hard Process

The hard scattering process is used to probe the distance scales below the radius of protons and is calculated including the phase space factor and the ME. The scattering cross section is defined as

$$\sigma = \int d\Phi_n(s, p_1, ..., p_n) \frac{|M|^2}{s} \tag{3.2}$$

In the above equation phase space factor is represented by Φ and is dependent on the energy of the incoming particles. The matrix element is summed over all the processes involved with identical final states. The example of a hard process is the W or Z production in association with jets and

these are processes which makes the main background analysis involving one or more jet. The cross section can be described on the basis of jet multiplicity as:

$$\sigma v + onejet = a_1\alpha_s + a_2\alpha_s^2 + a_3\alpha_s^3... \tag{3.3}$$

$$\sigma v + twojet = b_2\alpha_s^2 + b_3\alpha_s^3... \tag{3.4}$$

where V represents the Z or W boson.

Parton Shower
Parton showser actually provides a link between the differential cross section and the parton level. It is used

Hadronisation
Hadronisation is the last step, can be explored using MC simulation but once the parton shower has develped. The hadronisation is the process of formation of hadrons out of quarks and gluons. Because of the confinement can't exist separtely. The QCD of hadronisation is still not fully understood but the process is modeled in several hadronisational phenomenological studies. Two approaches exists to the hadronisation:

1. The string fragmentation model
2. The cluster fragmentation model

The string model is implemented in PYTHIA while cluster model is modeled in HERWIG.

3.3 Monte Carlo Generators

Several common MC generators are usually used in particle physics data analysis. They are used to sumilate the final state of any high energy collision. They contain a large library of hard the SM and Beyond the SM processes. A few applications of any event generator are:

1. It helps in planning for building of a new detetor to optimize the performance.
2. It is used as a tool for devising the analysis strategies used in future on real data taken the planned detector.
3. It gives a feeling of a real data before building a detector.

Some of them which are used in the $WW^*b\bar{b}$ analysis are described here:

1. POWHEG : The POWHEG stands for "Positive Weight Hardest Emission Generator", it is a computer program to generate events in hard pp colllision and it is accurate to next-to-leading order (NLO). $t\bar{t}$ and single top quark samples are generated with the POWHEG-Box using CT10 parton distribution function interfaced to PYTHIA6 [**?**].

2. SHERPA : It is a multi-purpose particle physics event generator. It provides a complete hadronic final states and the produced events may be passed into detector simulation used by several collider experiments. The whole code is written in C++ just like other generator i.e PYTHIA6, SHERPA is used in simulation of lepton-lepton, lepron-photon, photon-photon collisions. In this analysis SHERPA is used to generate the processes of W+jets, Z+jets and Dibosons.

3. PYTHIA : Just like SHERPA, PYTHIA is also a multi-purpose event generator and can simulate the collision between particles such as electorn-positron, proton-antiproton in various combinitions in the range of 10 Gev to 100 TeV, uses pertubative QCD for both low P_T and high P_T regions. In this analysis PYTHIA is used to simulate $t\bar{t}$, single-t interfaced to POWHEG.

4. HERWIG : Herwig is a multi-purpose particle physics event generator. It is built based on the experience gained with both the HERWIG 6 and HERWIG++ 2 event generators. Continuing the HERWIG++ 2 development, HERWIG 7.0 (HERWIG++ 3.0) replaces any prior HERWIG or HERWIG++ versions. In this analysis HERWIG++ is used signal sample.

CHAPTER 4

Data Acquisition and Data Processing in ATLAS

In this chapter I will describe the process and acquisition of data in the ATLAS experiment. Trigger is the piovat point of every hadron collider physics experiments. Its main technologies are discussed here.

4.1 Importance of Trigger

The trigger of any experiment behaves just like as a filter, as it filters only those events which are important for physics analysis out of a huge amount of events that take place in pp collisions.
The trigger system of ATLAS needs to meet few requirements:

1. Redundancy: During data taking it is necessary to disable any particular part of the trigger if the output rate is high enough or disturbs the rest of the data acquisition process.

2. Robustness: The running of the trigger should be stable otherwise technical problems could lead to a crash of the whole trigger system.

Apart from the above contraints the trigger system should have a trigger decision efficient and fast as process all the events within a frame of time allocated. Rate and efficiency are two important factors through which the performance can be quantified. The trigger system should be confirmed that the triggered events contains interesting physics and the discarded events were of no use.

4.2 The ATLAS Trigger System

The ATLAS trigger system is designed to catch a few hundered interested physics events for permanant storage and discard most of the unwanted events. It is one of the most important component of all the high luminosity experiments, such as ATLAS. In such type of experiments the rate of data produced is so high that is imppossible to record all of them as one event requires around 1.7 MB storage space. During Run-1, the rate of selected events was reduced from 20 MHz to 1kHz with rejection factor of the order of 20,000 [32]. This trigger system is divided into three levels as briefly described in the subsequent sections and a schematic view is shown in figure 4.1.

4.2.1 The Level-1 Trigger

The LVL-1 trigger of the ATLAS detector is the first stage of the trigger system which is responsible to reduce the initial 40 MHz rate to about less than 75 kHz. It is a hardware based trigger system which consists of the Central Trigger Processor (CTP), the L1Calo and L1Muon are the hardware systems uses reduced-granularity information to search for high transverse-energy electrons, photons and jets etc. As a result the output of this LVL1 system is a single bit called Level-1 Accept (L1A), which fed signal to the front-end readout systems using the Trigger Timing and Control system (TTC). The readout of the accepted events are then passed to the HLT. The LVL1 system takes only 0.5 micro seconds to decide whether to store or discard the events. For every data taking period the LVL1 is provided a trigger menu 250 items upon which dicision takes place. These items includes algorithms to trigger on jets, missing transverse energy, electrons and photons. By increasing the luminosity these trigger items are also increased.

4.2.2 The High Level Trigger

Unlike LVL1, HLT is a software based which is using information from all sub-detectors. HLT is the combination of LVL2 and the Event fillter (EF). In Run1 the LVL1 rate was 70kHz and an everage processing time was 75 ms/event. The LVL1 triggers are used to identify the Regions of Interest (RoIs) which are then ivestigated by the HLT as a second step. This mechanism dramatically reduces the relevant fiducial volume necessary to be readout and processed to the small regions guided by the hardware-based LVL1 trigger. The EF is based on offline algorithms and provides information to the Even Builder. It is used to collect data from the readout system PCs and provides fully assembled events to the EF. In Run1 the rate of EF was reduced to 700 Hz and the average processing time to 1 s/event.

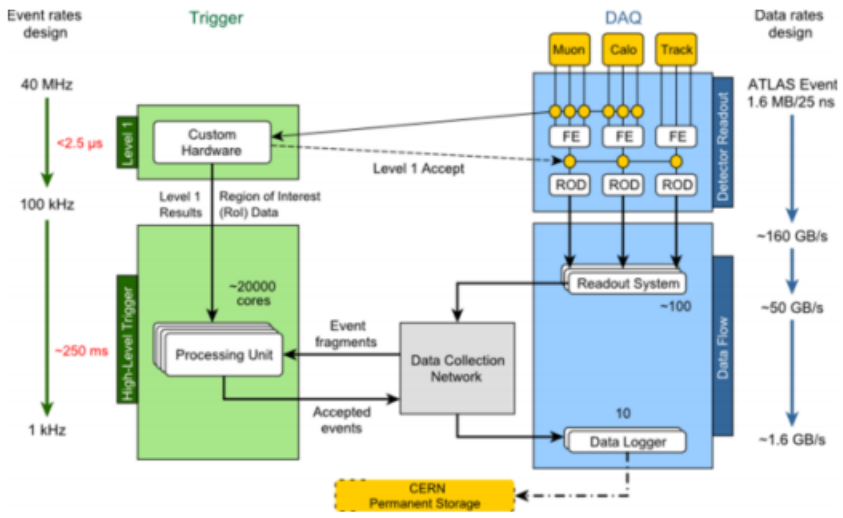

Figure 4.1: A diagram of the ATLAS trigger and data acquisition system.

To know more about trigger performance, it is crucialy important to know about the algorithm of trigger. For this reason jet, muon trigger and combined triggers are briefly explained as below:

Jet Trigger

The ATLAS LVL1 trigger is used to reconstruct jets, the triggered jets are usually composed by 2×2 blocks of trigger towers. A sliding window algorithm is used to combine them into proto-jets. If the energy of the LVL1 trigger jets is sufficient enough to pass the required threshold, the region of interest of the LVL1 is passed to LVL2. The algorithm of LVL2 is a cone clustering algorithm runs a limited number of iterations on calorimeter clusters in a rectangular region around the region of interest identified at the LVL1. During Run 1 the jet trigger performance was monitored and was modified in order to solve some specific performance issues. Two of them are:

- It was noticed that for multijet triggers the efficiency was not 100% and also the region of interest approach was insufficient in a busy multijet enviroment. Due to the reason that the L1 sliding window has a square size (in η and ϕ) while offline jets are circular. To address these issues a solution was found by running an anti$-kt$ algorithm and 100% efficiency was achieved. This is called L2 full scan.

- The original EF was efficient only above 60 GeV and goal was to access to low the Et region.

This issue was addressed by running the jet finding algorithm using only a fraction of data collected by a random L1 trigger at EF.

The jet event was increased in Run 2 because of the center-of-mass, luminosity and pileup and goal was to keep the trigger threshold as low as possbile. In Run 2, a new the L1 calorimeter hardware allowed pileup subraction event by event keeping the L1 threshold low. Since the first collision the ATLAS jet trigger has shown an excellent performance and a few improvement would be made in Run3. The upgrage of the ROS on increasing the density of the system as well as increasing the data rates. Moreover, due to the future expansion of the HLT the overall buffering capicity was also upgraded. Furthermore, the entire LVL2 structure has been simplified and two processing steps merged as shown in figure 4.2.

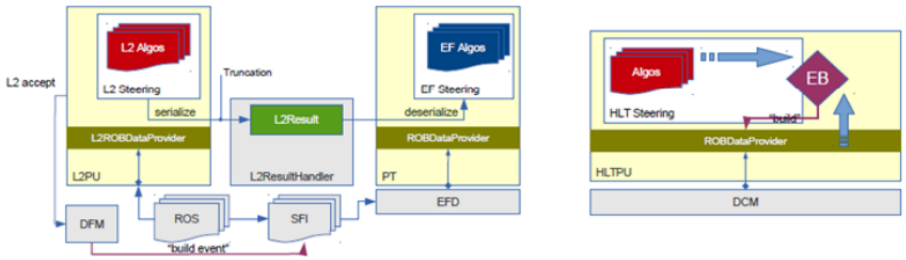

Figure 4.2: Run 1 HLT conceptual structure (left) alongside the Run 2 merged structure (right).

Muon Trigger

In the final state, events with muons are an important signatures for several analysis. An efficient trigger on muon along with its performance is of most important. In the ATLAS muons are triggered in a range of $|\eta|< 2.4$. The trigger coverage in the endcap is almost 100% while in the barrel it is lower because of beometrical acceptance due to crack around the mirror symmetry axis of the detector at η=0. For the timing resolution two of the four muon sub systems having good enough resolution are used for triggering. Muons are triggered by the LVL1 by finding a hit conincidence between different muon detector layers, using the RPC and TGC in the barrel and the end-cap regions respectively. At the L2, the L1 candidates are refined by the MS trigger chambers (RPC) and then they are combined with the tracks identified by the ID. EF uses two algorithms i.e outside-in and inside-out. In outside-in first MS information are combined with the ID traks and in outside-in strategy ID tracks are combined with MS iformation.

The accelerator went through several upgrades in a long shutdown one. The collision rate of LHC was 20MHz in Run 1 and was increased to design value of 40 MHz in 2015 as bunch space was increased from 25 to 50 ns in Run 2, the single lepton trigger rate was expected to increase by a factor of 4 compared to Run 1, resulted to various upgrades described below:

In Run 1 the LVL1 muon trigger was suffered from high fake rate i.e most of the fake muons were found in high η regions. This kind of triggers were reduced by introducing the conincidence between inner and outer TGC. This concidence reduced the fake rate by 80% while maintaining a muon efficiency of almost 100% in Run 2.

Electron Trigger

At the L1, electron clusters are triggers based on inputs from the calorimeter and the inner detector to build an Region of Interest consists of 4×4 trigger towers, azimuthal angle, analogue summation of energy in the calorimeter cells. The deposited energy with a hadronic layer is mearured by the calorimeter system while an inner detector electromagnetic layer. The LVL1 uses sliding window algorithm to identify a local energy maxima by using the overlapping towers within 2×2 region for the EM energy reconstruction. To discriminate hadron jets, it also computes the energy sum in the isolation ring formed by the surrounding 12 towers in the EM calorimeter as well as the hadronic core energy behind the 2×2 EM clustes. In Run 1 the L1 EM cluster Et threshold was dependent on pseudorapidity to take ino account the energy loss in the detector material before the calorimeter and a veto on hadronic core energy more than 1 GeV was also required for the main unprescaled EM triggers.

Upgrade of the LVL1 calorimeter brought many improvements during Run 1. The upgrade of the cluster Processor Module allows the definition of five Et dependent electromagnetic isolation selection with a precision of about 0.5 GeV. A new Multi Chip Module in the Pre-processor was responsible for the signal processing but now functioning a noise autocorrelation filter to get more better energy resolution. At the HLT, the full detector granularity is used within ROI for the final trigger decision and electrons are identified with the EM clusters with an additional tracks matching. A few modification were made at the HLT. The fast calorimeter reconstruction and selection was skipped in Run 2 while fast track reconstruction was run for electron triggers.

Combined Trigger

This section briefly explains the motivation of using combined triggers by explaining their advantages over single object triggers. Single object trigger can be combined in several ways to produce combined triggers. In combined triggers the reconstruction of objects used are same but only the hypothesis algorithm acts on the reconstructed object are replaced. The benefit of using combined triggers is that single objects triggers have relatively hight threshold then combined triggers. Due to this reason it allows high signal yield than single object triggers within the constraints imposed by the trigger system.

Combined triggers provides some disadvantages as well. The measurement of trigger efficiencies becomes more complicated. At least a two-dimensional binning is needed to accommodate for the two (or more) offline variables, and thus the turn-on curves have a higher dimensionality and more statistics is needed.

4.3 Physics Objects Reconstruction

At the LHC in pp collisions at the TeV scale, a large amount of different objects are produced possesses different energies. Those objects include photons, leptons and jets. The process in which these objects are produced includes both the SM and Beyond the Standard Model processes. Much efforts is required to disentangle prompt leptons and photons from the objects coming from jets and this is the only way to have more sensitive analysis less effected by background events.

In this chapter objects used in the $WWb\bar{b}$ analysiss will be discussed.

4.3.1 Track and Vertex Reconstruction

The ATLAS ID is the tracking system for charged particles only. Charged particles produce several hits while passing through the subdetectors of the Inner Detector. It consists of Pixel, SCT and TRT explained throughly in 2.3.1. Reconstruction of the primary vertices precisely is an important element of data analysis. The primary vertix is defined as

$$\sum_{i}^{N} (P_T^i)^2 \tag{4.1}$$

Where N is the number of associated tracks to the vertex and $(P_T^i)^2$ is the momentum of the i^{th} track. Tracks must pass the following requirements to be reconstruced as a vertex:

1. $|\eta|$<2.5 and p_T> 400 MeV
2. Hits in the first two pixel layers ≤ 1
3. Pixel holes = 0
4. SCT holes ≤ 1

The primary vertex reconstruction is divided in to two steps: vertex finding and vertex fitting. It consists of the follwing further steps:

1. The tracks must pass the selection criteria defined above
2. Position of seed is selected for the first vertex selected
3. Seed and tracks are used in fitting the vertex position
4. Once the vertex position is found, tracks are removed which are not compatible with the vertex. Vertex have atleaset two tracks.
5. This process is contiue untill no unassociated tracks are left.

4.3.2 Electron

To identify an electron, both information from the tracking system as well as from the calorimter of are used. Track match criteria is used i.e tracks produced in the ID and calorimeter cluster are combined to identify an electron, moreover the calorimeter shower profile is removed to be consitent with an EM shower. The variables used in the identification of an electron are the longitudinal and transverse shower profiles, the track quality, the track and cluster position.

Electron are identified within the range of $|\eta|< 2.47$, is the limit of the ID in $|\eta|$ and the region $1.37 < |\eta| < 1.52$ is called crack region. Electrons in this region are excluded from this analysis because infrastructure of cooling, a precise simultion of material is difficult.

To distinguish an electron from other particles produced with the collision, three levels of identification criteria are used. The identification levels are categorised as LooseLH, MediumLH and TightLH with 95%, 90% and 80% identification efficiency respectively. A likelihood-based electron identification tool has been adopted in the analysis to improve upon the cut based method of particle identification. The Loose likelihood regime uses variables useful for discrimination against light-flavour jets and electron conversions. In the Medium and Tight regimes, additional variables ($d0$, number of hits in the first pixel layers) are added for further rejection of conversions and

heavy-flavour jets.

Variables describing the longitudinal and lateral shapes of the EM showers in the calorimeters, the properties of the tracks in the ID, as well as the matching between tracks and energy clusters are used to discriminate against the different background sources. Table 4.3 summarizes which variables are used for the different selections so-called cut-based and likelihood (LH) identification menus. Electrons needs to be isloated and with this islolation criteria prompt electrons are selected and those are coming from hadron decays. Non−isolated electron candidates are also removed such as electron coming from the conversion of photons and light hadrons wrongly identified as an electrons. In this analysis, the isolation variable used for the reconstruction of electron is $Track$-based isolation, $P_T^{varcon0.2}$; sum of transverse momenta of all tracks which satisfies the quality requirements within a cone of $\Delta R = \min(0.2, 10\,\text{GeV})$ around the track of an electron candidate.

	Cut-based				Likelihood		
Name	Loose	Medium	Tight	Multilepton	LooseLH	MediumLH	VeryTightLH
$R_{\text{Had(1)}}$	✓	✓	✓	✓	✓	✓	✓
f_3		✓	✓	✓	✓	✓	✓
$W_{\eta 2}$	✓	✓	✓	✓	✓	✓	✓
R_η	✓	✓	✓	✓	✓	✓	✓
R_ϕ					✓	✓	✓
w_{stot}	✓	✓	✓	✓			
E_{ratio}	✓	✓	✓	✓	✓	✓	✓
f_1					✓	✓	✓
n_{Blayer}		✓	✓	✓	✓	✓	✓
n_{Pixel}	✓	✓	✓	✓	✓	✓	✓
n_{Si}	✓	✓	✓	✓	✓	✓	✓
d_0		✓	✓			✓	✓
σ_{d_0}						✓	✓
$\Delta p/p$				✓	✓	✓	✓
n_{TRT}		✓	✓	✓			
F_{HT}		✓	✓	✓	✓	✓	✓
$\Delta\eta_1$	✓	✓	✓	✓	✓	✓	✓
$\Delta\phi_2$			✓				
$\Delta\phi_{\text{res}}$				✓	✓	✓	✓
E/p			✓				
isConv			✓				✓

Figure 4.3: The variables used in the different selection of the electron identifies menu.

In this analysis electrons are required to pass the tight requirement criteria. Figure 4.2 and 4.3

shows the identification efficiency as a function of $|\eta|$ and missing Et at $\sqrt{s} = 8$ TeV and $\sqrt{s} = 13$ TeV.

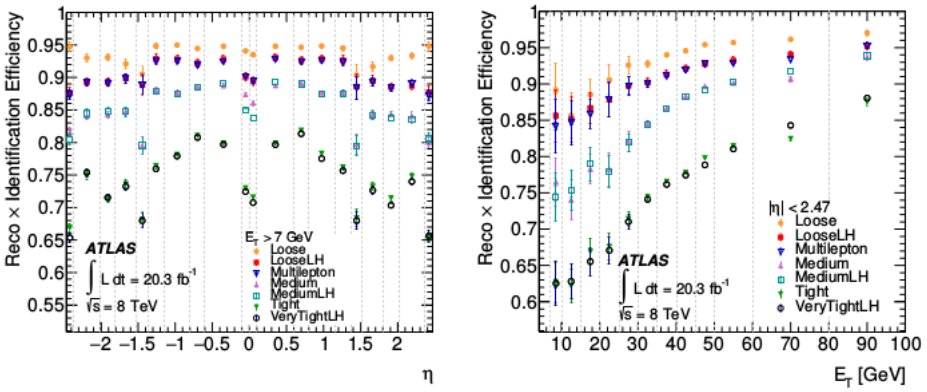

Figure 4.4: The two figures show the reconstruction and identification efficiency at likelihood electron and cut-based selection as a function of $|\eta|$ and missing Et at $\sqrt{s}$=8 TeV.

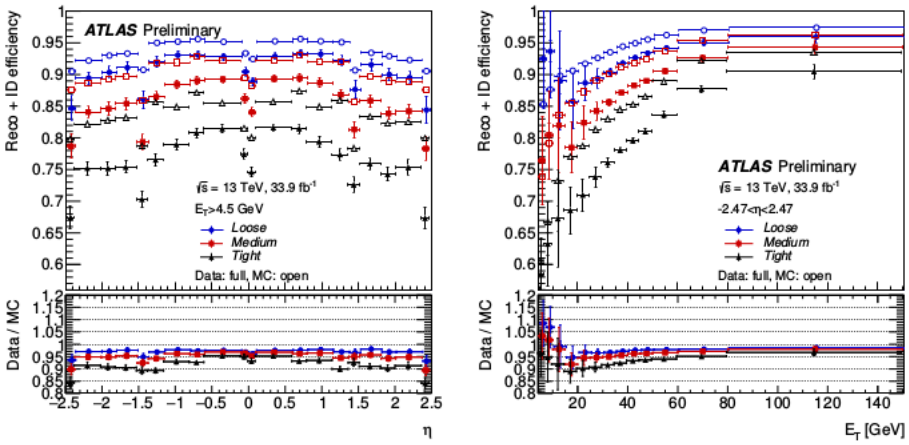

Figure 4.5: The two figures show the reconstruction and identification efficiency at likelihood electron and cut-based selection as a function of $|\eta|$ and missing Et at $\sqrt{s}$=13 TeV.

An additional cut significance of the transverse impact parameter ($|d_0^{sig}|$) is required and is fixed to be less than two standard deviation. Table 4.1 shows the electron selection.

Table 4.1: A set of electron selection requirement.

Electron Selection	p_T	$\|\eta\|$	**ID**	$\|d_0^{sig}\|$	$\|\Delta_0^{BL}\sin\theta\|$	Isolation
VHLooseElection	> 7 GeV	<2.47	LH Loose	< 10	< 0.5 mm	–
SignalElectron	> 27 GeV	< 2.47	LH Tight	< 2	< 0.5 mm	FixedCutTightTrackOnly

4.3.3 Muon

To reconstruct muon information from the ID and the MS detectors are used. In the pp collision muons are produced in energy range from 10 GeV to 1 TeV. Muon at this energy behave as minimum ionizing particles deposit a tiny amount of energy in the calorimeter [34]. To form a muon track infromations from individual subdetectors are collected [35]. They are reconstructed using different layers of the MS and then matched with the their respective tracks in the ID. The reconstruction process of muons follows the same steps as is done for the other charged particles i.e electron. To search for the hits on trajectory a Hough transform is used described in [38].

ATLAS defines four different types of muons depending on the usage of sub-detectors.

1. **Combined Muons :** Combined muons are those in which muon tracks are reconstructed independently in the ID as and in the MS. The combination of the trcks is performed with a global fit using informations from the ID and the MS. Combined muons have high purity in all physics analysis.

2. **Segmented Muons :** A muon is catagorized as a segment-tagged muon if the ID track is associated with at least one local track segment in the MDT chamber. Tagging algorithms are used to identify tracks by using a distinctive energy deposition pattern.

3. **Standalone Muons :** A track found in the ID and then it is extrapolated back to the beam pipe.

Just like electrons, muons possess three levels of identification quality i.e Loose, Medium and Tight with the corresponding identification efficiency of 95%, 90% and 80% respectively. Combined and Extrapolated muons are used for the loose selection. The Loose identification criteria are designed to maximise the reconstruction efficiency. The benefit of the loose muons selection is to maximise the reconstruction efficiency.

Combined and Extrapolated muons are qualify for the medium muons selection as well and this helps in minimizing the systematic uncertainity in muons calibration and reconsturction.

Tight muons are used to increase the purity up to 90% and only combined muons having hits in munimum of two stations of MS satisfy the medium muon requirent.

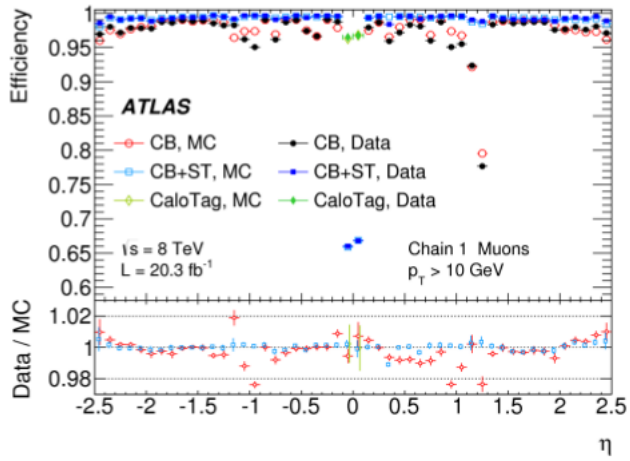

Figure 4.6: The figure shows the muon reconstruction efficiency as a function of $|\eta|$ measured in $Z \rightarrow \mu^+\mu^-$ events for muons with $P_T > 10$ GeV and measured using collision recorded with $\sqrt{s}$=8 TeV.

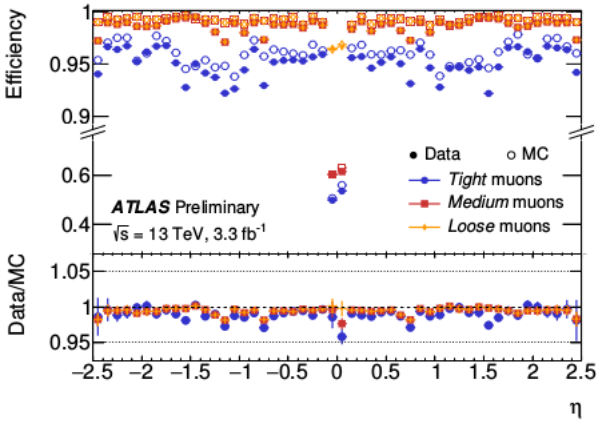

Figure 4.7: The figure shows the muon reconstruction efficiency as a function of $|\eta|$ measured in $Z \rightarrow \mu^+\mu^-$ events for muons with $P_T > 10$ GeV and measured using collision recorded with $\sqrt{s}$=13 TeV.

Muons candidates are selected within $|\eta|$<2.5. In this analysis medium quality criteria is used for the identification of muons. Figure 4.5 and 4.6 shows the efficiency of reconstruction for muons

having p_T up to 300 GeV at $\sqrt{8}$ TeV and $\sqrt{13}$ TeV respectively. Just like electrons, the same isolation variables are used in this analysis which include the track basd isolation, $P_T^{varcon0.2}$; the sum of transverse momentum of all tracks which satify the quality reauirement in this analysis within a cone of ΔR = 0.3, 10 GeV/pt. An additional cut significance of the transverse impact parameter ($|d_0^{sig}|$) is required and is fixed to be less then 6 standard deviation. A set of muon selection requirement are shown in table 4.2.

Table 4.2: A set of Muon selection requirement.

Muon Selection	p_T	$\|\eta\|$	**ID**	$\|d_0^{sig}\|$	$\|\Delta_0^{BL}\sin\theta\|$	Isolation
VHLooseMuon	$>$ 7 GeV	<2.47	LH Loose	$<$ 6	$<$ 0.5 mm	–
SignalMuon	$>$ 27 GeV	$<$ 2.47	Medium quality	$<$ 2	$<$ 0.5 mm	FixedCutTightTrackOnly

4.3.4 Jets

Jets behaves as a collimated sprays of hadrons, they appear in pp collisions due to the hadronization of quarks and gluons. Jets play an important role in several SM analyses. All stable particles having lifetime more than 10 ps, except neutrinos and muons, are used for the definition of jets in the simulation. Jets are reconstructed using only tracks originating from the primary vertex. In the ATLAS we use only jets reconstruction based on calorimeter deposits because of the limited acceptance of tracker acceptance. They are reconstructed using an anti-k_t algorithm[1] with radius parameter of 0.4 from three-dimensional topological electromagnetic clusters as an input. The topological clusters are groups of calorimeter cells. To reconstruct jets two inputs are needed.

- The clusters are seeded with a total energy $>4\sigma_{cell}$, where σ represents niose level. Neighbouring cells with noise level $> 2\sigma_{cell}$ are added to the cluster in order to increase its size.
- Input of noise-suppressed towers and Ghost-towers

Due to the application jet cleaning, jet algorithm is applied built from noisy calorimeter cells or non-collision background are removed. Jet Vertex Tagger [2](JVT) criteria (JVT $>$ 0.59) is applied to jets with $p_T <$ 60 GeV and $|\eta|$<2.5 in-order to avoid to select jets originating from pile-up.

Jet initiated by b-quark are defined b-jet in this thesis. Signal jets are those which passes the JVT requirement with $p_T >$20. As specified in the table 4.3 along with other specifications, MV2c10

[1]The anti-k_t is a clustering algorithm produces jets in a circular shaped.
[2]The Jet Vertex Tagger gives the measurement of number of tracks associated with the jet coming from the primary vertex.

algorithm; jet flavor tagging algorithm is used to suppress multijet, W+jet and Z+jet backgrounds and select signal jets.

Table 4.3: Jet selection requirement with distance paramter R = 0.4.

Requirement	Signal Jets
p_T	anti-k_t
$\|\eta\|$	20 GeV
Quality	< 2.5
Pile-up jet removal	not bad jet
b-tagging	MV2c 10, 85% fixed-cut Working point

4.3.5 Missing Transverse Momentum

The missing transverse momentum is used to estimate the transverse momentum of an assumed neutrino originating from a W decay. The MET is measured using the objects like electrons, jets and muons as briefly explained in sections 4.3.2, 4.3.3 and 4.3.4. A track-based algorithm [37] is used for the calculation of the MET. Figure 4.8 shows the resolution of the track-based algorithm as a function of $\sum E_T$ in a sample of $Z \to \mu\mu$.

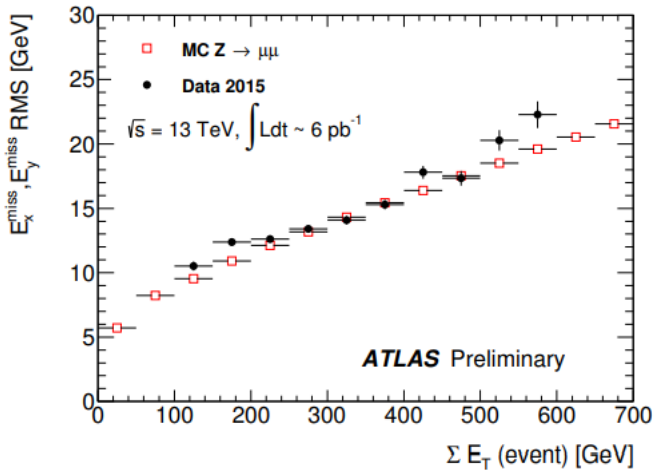

Figure 4.8: Resolution of the missing transverse energy calculation as a function of $\sum E_T$ in $Z \to \mu\mu$ events at $\sqrt{s}$=13 TeV.

CHAPTER 5

Higgs Boson Pair Production in $WWb\bar{b}$ Final State

The process discussed in this work is the pair production of Higgs bosons with the following decays to $b\bar{b}$ and WW^*. The two W's can decay in a quark, anti-quark pair or to a lepton plus neutrino ($l\nu$), where l is either an electron or muon. Unfortunately the final state $WWb\bar{b}$ is also produced in the top anti-top quark ($t\bar{t}$) decay. In fact top quark can decay to w^+b^- and anti-top quark to w^-b^-. Therefore the separation between signal and background is very challanging. Nevertheless there are several variables that can be used to separate signal from background, these varaibles exploit the kinematic differences due to the Higgs boson mass, the top quark mass and the different m_{wwbb} distributions. The $t\bar{t}$ is the main background because it imitates the signal topology. Schemes of the hh and $t\bar{t}$ decays are shown in figure 5.1.

For hh, the $b\bar{b}$ pair comes from the h decay, therefore the mass of the bb system is almost equal to the mass of the Higgs boson, there is also a small angular separation between the two $b's$ and the two $W's$. In the $t\bar{t}$ case, the two b's are far apart as well as the $W's$, therefore they have a large angular separations (ΔR). The angular separation between two particles is defined through the variable $\Delta\mathrm{R} = \sqrt{(\Delta\phi)^2 + (\Delta\eta)^2}$ where $\Delta\phi$ and $\Delta\eta$ are the differences between the azimuthal angles and pseudorapidities of the two particles.

In addition to the $t\bar{t}$ background, also other less relevant backgrounds are considered. One of them is the W boson production in an association with jets. The quark anti-quark pair collides producing the W boson which further decays to one lepton and neutrino. Due to the initial state radiations the quark produces quark, anti-quark pair further creating two jets. These can be light jets or b-jets. The only difference between the W and the Z bosons production is that the Z boson decays to two

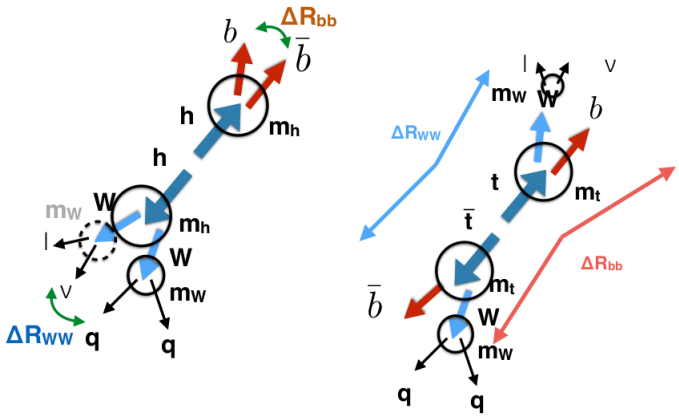

Figure 5.1: Schematic diagram of the $t\bar{t}\to l\nu qqb\bar{b}$ decay (main background) and $hh\to l\nu qqb\bar{b}$ decay (signal).

leptons instead of lepton neutrino pair in order to conserve charge. Both of these backgrounds have very high cross sections. The other background is Diboson that includes the W^+W^- and the ZZ bosons. The W^+ decays to lepton and neutrino and the W^- creates two light jets in an association with the $b\bar{b}$ pair while the ZZ decays to two leptons and two light jets in an association with the $b\bar{b}$ pair. Table 5.1 summarizes the background samples cross-section and the respective generators for all backgrounds at center-of-mass of $\sqrt{s}$ = 13 TeV. The signal is normalized to $\sigma(pp\to hh)$ $\times 2\times$ $\mathrm{Br}(h\to b\bar{b})\times\mathrm{Br}(hh\to W^+W^-)$.

Table 5.1: The cross-sections for the signal and background processes at $\sqrt{s}=13$ TeV center-of-mass energy. The number of events is normalized to 36.1 fb^{-1}.

Process	σ_{13TeV}(pb)	**Number of Events**	**Generator**
$t\bar{t}$	831	29999×10^3	POWHEG+PHYTHIA6
Single t, t-channel	68	2448×10^3	POWHEG+PHYTHIA6
Single w, w-channel	67	2412×10^3	POWHEG+PHYTHIA6
Single s, s-channel	3	108×10^3	POWHEG+PHYTHIA6
Diboson	11	403×10^3	SHERPA
Z+jets	19979	719244×10^3	SHERPA
W+jets	20080	722880×10^3	SHERPA
Signal	40.01	1584×10^3	Madgraph5_aMCatNLO+Herwig++including Form Factor

5.1 Monte Carlo Samples

Samples of simulated signal and background events were used to design the event selection, estimate the signal acceptance and the background yields from the various SM processes.

The sample for single top quark and the $t\bar{t}$ are generated with the POWHEG-Box v2 using the CT10 parton distribution function interfaced to PYTHIA 6.428 for parton shower. The mass of the top quark is set at $m_t = 172$ GeV. One of the two top quarks is required to decay to a final state with only one lepton and the cross section of the $t\bar{t}$ is known to NNLO in QCD. The t, s and Wt-channels are generated separately and their cross section is calculated as described in [40]. SHERPA v2.21 [41] is used as a baseline generator for the W+jets and the Z+jets background events. All the diboson (ZZ, WW, WZ) processes are generated with SHERPA with the CT10 PDF set. Signal samples were generated using MADGRAPH5_aMC@NLO interfaced to HERWIG++ according the procedure described in [39] at next to leading order (NLO). Events were generated with an effective Lagrangian in the infinite top-quark mass approximation, and were reweighted the generated events with from factors that take into account the finite mass of the top quark.

5.2 Trigger Selection

Events were selected using the triggers shown in table 5.2, they require the presence of at least one electron or one muon in the final state, and they were all unprescaled. For each row in the table events were selected with a logical OR among all triggers appearing in that row. The rows of the table correspond to different acquisition periods: namely period A, B, D and E, which are further divided into subperiods. Specific subperiods have similar trigger configurations. In the following we describe the trigger items shown in the table:

- The `mu20_iloose_L1MU15` trigger requires a muon of P_T larger than 20 GeV at HLT, in addition the `iloose` isolation criteria is applied cutting on $p_T^{cone0.2}$. The isolation variable $p_T^{cone0.2}$ is defined as the sum of the P_T of tracks having P_T>1 GeV found in the ID in a cone of ΔR = 0.2 around the muon candidate, after subtracting the P_T of the muon. The HLT trigger is seeded by the LVL1 trigger `L1MU15` asking for muon of P_T larger than 15 GeV;

- The trigger `mu24_ivarmedium` is asking for a muon of P_T larger than 24 GeV while `ivarmedium` is an isolation cut dependent on the muon P_T: $\frac{\sum P_T^{trk}}{P_T}$<0.07 in a ΔR<0.3 cone;

- The `e26_lhtight_nod0_ivarloose` trigger requires an electron of E_T larger than 26 GeV. The event selection uses a single electron trigger with likelihood tight identification requirement as described in section 4.3.2, no cut on the transverse impact parameter is applied while

`ivarloose` stands for an isolation dependent on the electron P_T: $\frac{\sum P_T^{trk}}{P_T}$<0.1 in a ΔR<0.2 cone;

- The trigger `e24_lhmedium_L1EM18VH` requires an electron candidate with E_T >24 GeV satisfying the `lhmedium` identification. The `lhmedium` refers to the likelihood medium identification criteria applied on electrons. This trigger is seeded by the `L1` trigger `L1EM18V`. The `L1EM18VH`, is the `L1EM` trigger with P_T larger than 18 GeV of energy deposited in the electromagnetic calorimeter, while `VH` refers to an additional requirement on the L1 trigger where `V` indicates a variable threshold for hadronic isolation;

- The `e120_lhloose` trigger asks for an electron of E_T larger than 120 GeV and the electron must satisfy the likelihood loose identification criteria. Electron have to pass a $|\eta|<$ 2.5 cut;

- The trigger `e60_lhmedium_nod0` belongs to the acquisition period 2016-A, it requires an electron of E_T larger than 60 GeV while `lhmedium` is the likelihood medium electron selection and no $d0$ impact parameter is required;

- The `mu24_iloose` trigger requires a muon of P_T larger than 24 GeV at HLT, in addition `iloose` isolation criteria is applied cutting on $p_T^{cone0.2}$;

- The `e60_lhmedium` requires an electron of E_T larger than 60 GeV and `lhmedum` is the likelihood medium identification criteria;

- The trigger `mu50` asks for a muon of P_T larger than 50 GeV. It has been used in all periods except 2016-A, where its threshold has been decreased to 40 GeV due to a problem in the trigger configuration that disabled the trigger `mu50`;

- The `e60_lhmedium_nod0` trigger belongs to an acquisition period 2016 D4-E3, requires an electron candidate with E_T larger than 60 GeV satisfying the likelihood-based identification, no transverse impact parameter is applied;

- The `e140_lhloose_nod0` trigger is asking for an electron of E_T larger than 140 GeV, `lhloose` is the likelihood loose identification requirement and no impact parameter is required;

- The `e60_lhmedium_nod0` trigger requires an electron of E_T larger than 60 GeV while `lhmedium` is the likelihood medium identification criterian and no impact parameter is required;

- The `mu24_iloose` trigger requires a muon of P_T larger than 24 GeV satisfying the `iloose` identification criterian;

- The `e140_lhloose_nod0` trigger is asking for an electron of E_T larger than 140 GeV while `lhloose` is the likelihood identification selection requiring no impact parameter;

- The `mu26_ivarmedium` belongs to the data acquisition period D4-E3 of year 2016. This trigger requires a muon of E_T larger than 26 GeV while `ivarmedium` is the isolation dependent on P_T of muon and the `medium` is the muon identification selection;
- Electron candidate events were selected using trigger `e120_lhloose` which requires one electron with a transverse momentum threshold of 120 GeV and loose likelihood identification criteria were used;
- The `e300_etcut` trigger requires one electron with transverse momentum higher than 300 GeV;

Table 5.2: Table shows the summary of triggers items used for 2015 and 2016 data. All the listed triggers are unprescaled.

Dataset	**Trigger Items**
2015	mu20_iloose_L1MU15 mu50 e24_lhmedium_L1EM18VH (MC) e24_lhmedium_L1EM20VH (data) e60_lhmedium e120_lhloose
2016 - A	mu24_iloose_L1MU15 (MC) mu24_iloose (data) mu40 e26_lhtight_nod0_ivarloose e60_lhmedium_nod0 e60_medium e140_lhloose_nod0 e300_etcut
2016 - Period B-D3	mu24_ivarmedium mu50 e26_lhtight_nod0_ivarloose e60_lhmedium_nod0 e60_lhmedium e140_lhloose_nod0 e300_etcut
2016 - Period D4-E3	mu26_ivarmedium mu50 e26_lhtight_nod0_ivarloose e60_lhmedium_nod0 e60_lhmedium e140_lhloose_nod0 e300_etcut

5.3 Event Preselection

In order to ensure good data quality, to select event with topology closer to the signal of interest and to pre-filter the most dominant backgrounds, a "pre-selection" has been defined. The pre-selection criteria are explained below and are applied on the objects used in the analysis before any cut is applied on them:

1. To ensure good data quality, events with bad detector conditions, namely where large part of the detectors were missing from the data taking due to problems during a run, have been rejected from the data analysis. Events with bad detector informations and imcomplete events are rejected.

2. The presence of a primary vertex with at least two tracks. Among all primary vertices, that with the highest $\sum {P_{T,trk}}^2$, where $P_{T,trk}$ is the transverse momentum of tracks associated with the vertex, is retained as the primary interaction vertex;

3. we require one lepton which should be either an electron or a muon satisfying the selection criteria. All objects (leptons and jets) must be matched to the corresponding HLT object which fires the trigger. The selections, applied to define the physical objects used in the analysis, are reported below:
   Electron Selection :

   - $P_T > 27\ GeV$: A selection on lepton P_T is performed to remove most of the non-prompt leptons, coming from the hadron semileptonic decays, generally having low transverse-ment momentum. The 27 GeV is choosen in order to select lepton passing the single lepton requirement;
   - $|\eta| < 1.37\ \&\ 1.52 < |\eta| < 2.47$: the region $|\eta| < 2.47$ corresponds to the fiducial acceptance of the EM calorimeter. Electrons with η falling in the crack region, $1.37 < |\eta| < 1.52$ are rejected because they have high miss identified electrons fraction;
   - $\frac{d_0}{\sigma_{d0}} < 10$: this variable represents the significance on the on the impact parameter d_0, defined in section 4.3.2, to reject non-prompt electron background;
   - $|\Delta Z_0^{IBL} sin\theta| < 0.5\ mm$: this selection allows to select electrons coming form the primary vertex, requiring that the longitudinal distance of the impact parameter from the primary vertex is very small;
   - *isolation Loose*: this working point corresponds to the looser isolation requirement as described in section 4.3.2;

Similary for muons the following requirements are used:

Muon Selection :

P_T> 27 GeV, $|\eta|$< 2.4, $\frac{d_0}{\sigma_{d0}}$< 10, $|\Delta Z_0^{IBL}\sin\theta|$< 0.5 mm, isolation Loose;

4. we require four jets in total and only two of them should be b-tagged satisfying object selection reported below;

   A P_T greater than 20 GeV, $|\eta|$< 2.5, the 85% b-tagging Fixed-Cut5 working point (WP) is selected to keep the signal efficiency high;

5.3.1 Event Reconstruction

Events are reconstructed by first requiring exactly two 2 b-tag jets, at least 2 light jets and at most 3 light jets. In three jet events, the jets from the W decay are identified as the highest P_T jet and the subleading P_T jet closest in ΔR to it.

The event kinematics of the $h \rightarrow WW \rightarrow lvqq$ topology is fully reconstructed. Only one component, the neutrino longitudional momentum is unkown among all four-momenta of the final state particle, it can be determined from the Higgs boson mass using the following relation:

$$m^2_{h\rightarrow WW*} = (p^l + p^v + p^{j1} + p^{j2})^2 \tag{5.1}$$

where p^l, p^v, p^{j1} and p^{j2} are the four-momenta of the selected lepton, the neutrino and the jets respectively. The mass of the $h{\rightarrow}WW^*$ system is set to 125 GeV. The neutrino longitudinal momentum (p_z) can be reconstructed. Additing to Eq 5.1 the following relation:

$$\begin{aligned} E^v &= \sqrt{(p_x^v)^2 + (p_y^v)^2 + (p_z^v)^2} \\ P_x^v &= E_{Tx}^{miss}, P_y^v = E_{Ty}^{miss} \end{aligned} \tag{5.2}$$

where E^v is the neutrino energy, p_x^v and p_y^v are the two transverse spatial components of the neutrino momentum (E_T^{miss}). The equation 5.1 is a quardatic equation in p_z having two real, one real or two complex solutions. When two complex solutions are found, the real part of is taken as the neutrino p_z.

In figure 5.2 and 5.3 all kinematic distributions for the non-resonant analysis are shown after preselction comparing background and signal. The shapes of the signal and background are different

and such differences are exploited to remove background events and increase the statistical significance of the analysis. In the figures the signal has been scaled up by a factor of 1000 times for presentation purpose. Following these considerations, the typical separation variables used are:

1. the p_T of the $b\bar{b}$ pair (p_T^{bb}): In order to evaluate the modeling of b-tagged jets, the background simulation is compared with the signal. The p_T^{bb} figure shows a broad peak around 70 GeV, then sharply goes down having a long tail while the signal is flatens under the 10000 number of events ending around 250 GeV;

2. the p_T of the WW pair (p_T^{WW}): The p_T^{WW} figure shows a peak around 80 GeV, while the signal is flate in that region with tail up to 350 GeV;

3. the ΔR of the WW pair system (ΔR^{WW}): The distribution shows the angular separation between the two W's. The $t\bar{t}$ distribution has a peak aroud 3 while the signal peaks at low values with a tail up to 3;

4. the ΔR of the $b\bar{b}$ system (ΔR^{bb}); The signal and background distributions behaves as described in the previous bullet. The ΔR is shown in figure 5.1;

5. the invariant mass of the dihiggs boson system (m_{hh}): The m_{hh} distribution shows a peak around 400 GeV and then sharply goes down ending at 1500 GeV. The signal distribution follows the same shap as that of the background distributions;

6. the invariant mass of the two b-jet system (m_{bb}): The m_{bb} distribution is plotted between 0 and 500 GeV. The distribution has a large peak around 100 GeV and then sharply goes down ending at 500 GeV while the signal has peak between 50 to 150 GeV indicating the higg boson mass;

7. the mass of the WW system, computed using the neutrino longitudinal momentum. This variable is exactly equal to the Higgs boson mass if a real solution for the p_z is found, otherwise it is larger than that;

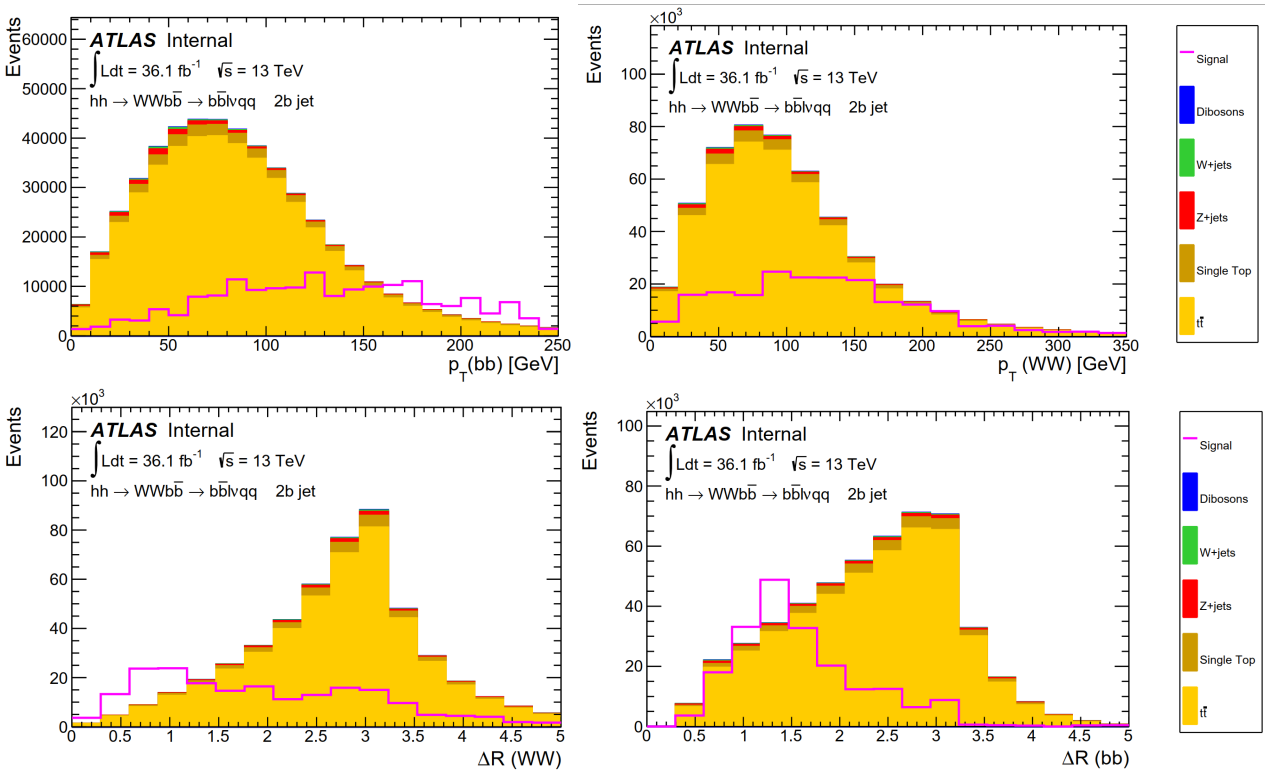

Figure 5.2: Distributions of the kinematic variables used in the analysis after preselection. The signal has been scaled by a factor of 1000 for a presentatino purpose. The top left is the P_T distribution of the bb system while top right is the P_T distribution of the WW system. Bottom left is the angular seperation distribution between the WW system while bottom right is the angular seperation distribution between the bb system.

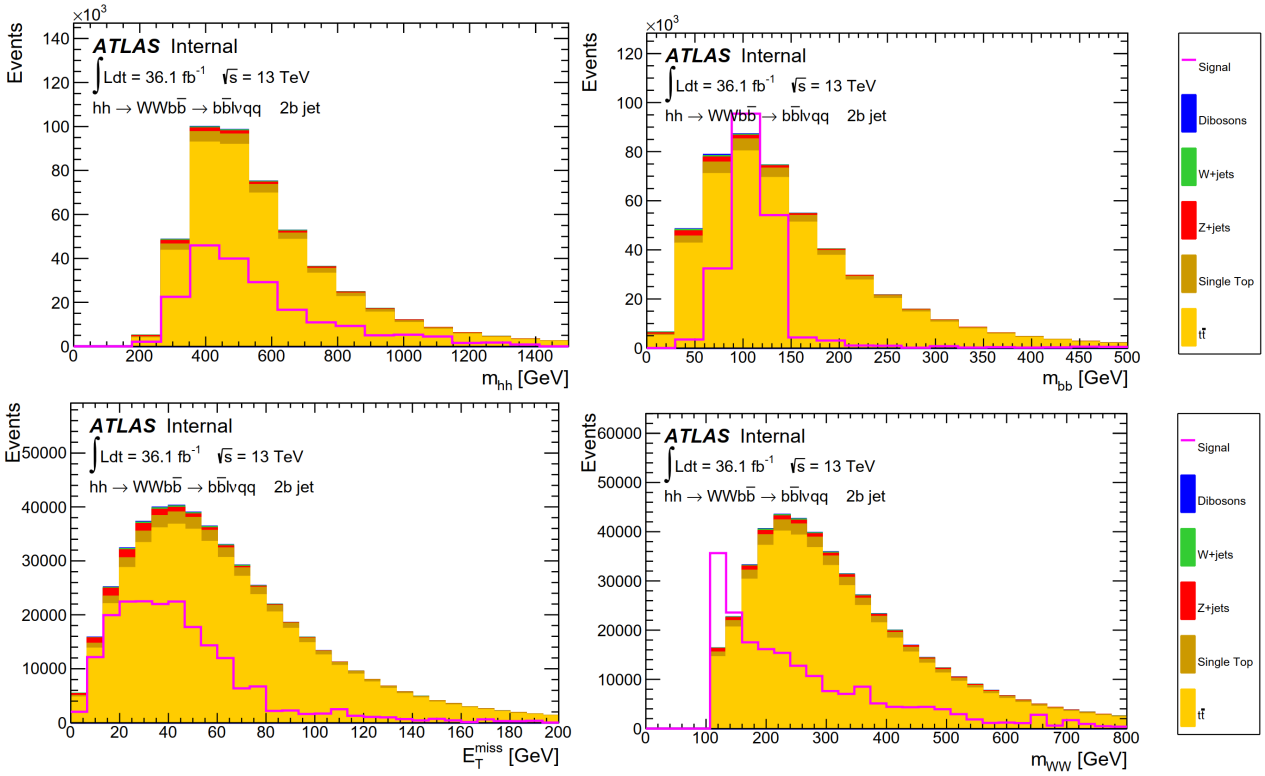

Figure 5.3: Distributions of the kinematic variables used in the analysis after preselection. The signal has been scaled by a factor of 1000 for a presentation purpose. The top left is the distribution of the hh system while top right is the mass distribution of the bb system. Bottom left is the distribution of the missing transverse energy while bottom right is the mass of the WW system.

5.3.2 Kinematic Selection Optimization

The kinematic selections were optimized to suppress background events while keeping the signal efficiency as high as possible. The optimization was performed by varying cuts on the main kinematic distriminating variables in predefined ranges evaluated looking qualitatively at the distributions shown in figure 5.2 and 5.3. The cuts on the variables were chosen to minimize the expected upper limit on the signal cross-section.

The following expression is used to compute the upper limit on the signal events at 95% CL

$$\sigma_{S(@95\%CL)} = \frac{1.64\sqrt{B + (0.3 * B)^2}}{\epsilon_S \mathcal{L}} \tag{5.3}$$

That corresponds to the upper limit in the infinite statistics limit $B >> 1$. Where B is the total number of expected background events, while 0.3 is the fractional systematic uncertainity on the background. The expression is obtained by summing in quadrature the statistical error on the background $\sqrt{B}$ and the systematic error on it (0.3 B) while ϵ_s is the signal acceptance of the luminosity used to normalise the samples.

The result of the optimization points to a P_T of the bb system larger than 300 GeV, the P_T of the WW system larger than 250 GeV and mass of the WW system less than 130 GeV, while m_{bb} must be in the range 105 to 135 GeV. Moreover, the missing transverse momentum is required to be greater than 25 GeV. The ΔR_{WW} and ΔR_{bb} resulted to have a marginal impact on the analysis sensitivity therefore cuts on these variables were not applied. Moreover, any cut on m_{hh} was not applied because the m_{hh} distribution is similar between signal and background as shown in figure 5.3. Table 5.3 and 5.4 show the number of observed and background events obtained after each selection cut. The events are triggered using single electron and single muon triggers.

Table 5.3: The number of observed events and expected background events for non-resonant selection using single muon triggers. No NF has been applied to the background yields. Only statistical uncertainties are shown. Preselection is to pre-filter the most dominant backgrounds, is as explained in section 5.3. N_Jet is the number of jets, N_Jet^{Cen} is the number of jets in the central part of the detector. The m_{WW} is mass of the WW system. The P_T(bb) and P_T(WW) are cuts on the transverse momentum of the two bb and WW systems. The m_{bb} is the invariant mass of the 2 b-jets.

Sample	**Preselection**	N_Jet**>4**	N_Jet^{Cen}**<3**	b**-jets≥2**	E_T^{miss}**>25**	m_{WW}**<130**	P_T^{WW}**>250**	P_T^{bb}**>300**	m_{bb}
Signal	16.9	16.8	14.9	8.78	7.26	0.91	0.14	0.05	0.04
Diboson	4.36e+04	4.32e+04	3.46e+04	4.76e+03	3.88e+03	86.3	4.14	1.14	0
W+Jets	1.91e+06	1.82e+06	1.33e+06	1.28e+05	1.06e+05	2.64e+03	62.6	12.8	2.01
Z+Jets	3.6e+05	3.45e+05	2.54e+05	3.08e+04	1.95e+04	849	10	2.08	0.15
Single Top	4.81e+05	4.8e+05	3.57e+05	1.49e+05	1.28e+05	2.69e+03	87.3	20	1.11
$t\bar{t}$	2.2e+06	2.2e+06	2.01e+06	1.21e+06	1.06e+06	2.01e+04	390	51.8	9.95
Total	4.99e+06	4.89e+06	3.98e+06	1.53e+06	1.31e+06	2.64e+04	554	87.8	13.2

Table 5.4: The number of observed events and expected background events for non-resonant selection using single electron triggers. No NF has been applied to the background yields. Only statistical uncertainties are shown. Preselection is to pre-filter the most dominant backgrounds, is as explained in section 5.3. N_Jet is the number of jets, N_Jet^{Cen} is the number of jets in the central part of the detector. The m_{WW} is mass of the WW system. The P_T(bb) and P_T(WW) are cuts on the transverse momentum of the two bb and WW systems. The m_{bb} is the invariant mass of the 2 b-jets.

Sample	**Preselection**	N_Jet**>4**	N_Jet^{Cen}**<3**	b**-jets≥2**	E_T^{miss}**>25**	m_{WW}**<130**	P_T^{WW}**>250**	P_T^{bb}**>300**	m_{bb}
Signal	15.3	15.3	12.4	7.49	6.27	0.7	0.08	0.03	0.02
Diboson	4.53e+04	4.48e+04	3.31e+04	4.38e+03	3.49e+03	64.6	2.7	0.7	0.02
W+Jets	1.71e+06	1.6e+06	1.02e+06	1e+05	8.14e+04	1.93e+03	31.3	5.07	0.89
Z+Jets	4.42e+05	4.2e+05	2.69e+05	2.48e+04	1.54e+04	521	6.59	1.73	0.15
Single Top	4.74e+05	4.72e+05	3.26e+05	1.36e+05	1.17e+05	2.13e+03	55.5	15.1	0.85
$t\bar{t}$	2.16e+06	2.16e+06	1.84e+06	1.11e+06	9.62e+05	1.7e+04	342	39.7	7.14
Total	4.84e+06	4.69e+06	3.48e+06	1.37e+06	1.18e+06	2.17e+04	439	62.3	9.08

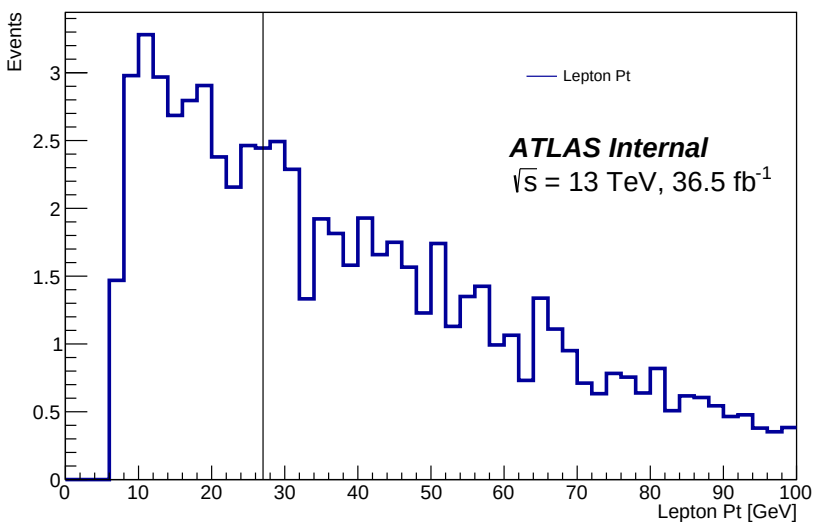

Figure 5.4: The P_T distribution of lepton without any trigger applied. The vertical line represents the threshold of single lepton trigger i.e 27 GeV.

5.4 Single Lepton Trigger Efficiency Study

In the standard analysis events are triggered with single lepton trigges, they require a lepton with P_T larger than 27 GeV. Figure 5.4 shows the P_T distribution of the lepton. From this distribution it is clear that large part of the signal events have a P_T lower than 27 GeV, not passing the trigger threshold 27. These events are 38$\pm$0.02% of the total. In table 5.5 and 5.6 the efficiency of the cuts used in the analysis without any trigger requirement for muon and electron are presented for the signal and the $t\bar{t}$ sample respectively. Unfortunately the efficiency for signal is very low because due to the large $t\bar{t}$ yield the analysis selection is very tight. Nevertheless the gain in S/B is large as can be seen in table 5.6. In both tables the last row is the efficiency of the m_{bb} selection with additional requirement of a single lepton trigger, where it is visible the 58% reduction of the trigger efficiency due to this requirement. It is therefore needed to add triggers that allow to lower the lepton P_T threshold. This can be achieved using multiobject triggers that select events with a concidence among different trigger objects. This allows to reduce the event rate compensating for the higher rate allowing to lower the lepton P_T threshold to 15 GeV. Two triggers are considered: the first trigger requries one electron with P_T larger than 15 GeV and the second trigger requires one muon with P_T larger than 14 GeV. And both triggers require the presence of three jets with P_T larger than 20 GeV as well. These triggers are briefly described below:

Table 5.5: Efficiency of the selection used in the analysis. Up to the 9th row no trigger is applied, at the last row single lepton trigger is applied.

Selection	**Muon channel**	**Electron channel**
Preselection	1.4×10^{-01}	1.1×10^{-01}
$N_{Jet}>4$	1.4×10^{-01}	1.1×10^{-01}
$N_{Jet}^{Cen}<3$	1.3×10^{-01}	9.3×10^{-02}
b-jets≥2	4.7×10^{-02}	3.6×10^{-02}
$E_T^{miss}>25$ GeV	3.5×10^{-02}	2.6×10^{-02}
$m_{WW}<130$ GeV	4.6×10^{-03}	3.6×10^{-03}
$P_T^{bb}>250$ GeV	2.7×10^{-04}	2.0×10^{-04}
$P_T^{ww}>300$ GeV	2.0×10^{-04}	1.3×10^{-04}
m_{bb}	1.8×10^{-04}	1.9×10^{-04}
Trigger+m_{bb}	7.04×10^{-05}	7.0×10^{-05}

Table 5.6: Efficiency of the selection used in the analysis using $t\bar{t}$ sample. Up to the 9th row no trigger is applied, at the last row single lepton trigger is applied. The 3rd and 4th column shows the ratio of the number of events for signal over background for muon and electron channels.

Selection	**Muon channel**	**Electron chnnel**	S/B	S/B
Preselection	1.8×10^{-01}	1.5×10^{-01}	1.5×10^{-5}	1.3×10^{-5}
$N_{Jet}>4$	1.8×10^{-01}	1.5×10^{-01}	1.4×10^{-5}	1.3×10^{-5}
$N_{Jet}^{Cen}<3$	1.6×10^{-01}	1.2×10^{-01}	1.4×10^{-5}	1.3×10^{-5}
b-jets≥2	9.9×10^{-02}	7.7×10^{-02}	8.4×10^{-5}	8.7×10^{-5}
$E_T^{miss}>25$ GeV	8.7×10^{-02}	6.7×10^{-02}	7.5×10^{-5}	7.2×10^{-5}
$m_{WW}<130$ GeV	4.1×10^{-04}	3.01×10^{-04}	2×10^{-03}	2×10^{-03}
$P_T^{bb}>250$ GeV	1.2×10^{-06}	9.8×10^{-07}	3×10^{-03}	3×10^{-03}
$P_T^{ww}>300$ GeV	8.3×10^{-07}	5.5×10^{-07}	4×10^{-03}	4×10^{-03}
m_{bb}	8.07×10^{-07}	4.6×10^{-07}	4×10^{-03}	4×10^{-03}
Trigger+m_{bb}	6.1×10^{-07}	4.3×10^{-07}	2×10^{-03}	2×10^{-03}

1. The `HLT_e15_lhtight_iloose_3j20_L1EM13VH_3J20` trigger requires an electron candidate with E_T larger than 15 GeV satisfying the `lhtight` identification criteria (see section 5.2) applied on electron, in addition `iloose` isolation criteria is applied. The trigger is seeded by the LVL1 triggers `L1EM13VH`. The `L1EM13VH`, is the `L1EM` trigger with P_T larger than 13 GeV of energy deposited in the electromagnetic calorimeter, while `VH` refers to an additional hadronic isolation requirement on the `L1` trigger. The trigger also requires three jets with P_T larger than 20 GeV. A sliding window algorithm is used to define L1 jets from a grid of jets elements, a block of calorimeter cells spanning 0.2×0.2 in projective $\eta\times\phi$ space. L1 jets are 4×4 collections of these jet elements, where the energy in the 2×2 core is a local maximum [42].

2. The `HLT_mu14_iloose_3j20_L1MU10_3J20` trigger requires muon candidate with P_T larger

than 14 GeV satisfying the `iloose` isolation (see section 5.2). The trigger is seeded by the LVL1 trigger `L1MU10`. The `L1MU10`, is an `L1` trigger asking for a muon of P_T larger than 10 GeV. The trigger also requires three jets with P_T larger than 20 GeV.

In order to evaluate the efficiency of the lepton plus jets triggers, the analysis selection has been modified lowering the lepton threshold to 14 GeV. In table 5.7 and 5.8 trigger efficiencies are shown for signal muon and electron channels respectively. The trigger efficiencies are computed at each selection step of the event in the analysis and they are reported for the single lepton trigger, single lepton plus three jets trigger and the logical "OR" between the two. This efficiency is obtained by the event yield passing the ratio of the specific selection without the trigger requirement and the same selection with the trigger requirement. The relative efficiency gain of the single lepton plus three jets trigger over the single lepton trigger is shown in the last column of the two tables.

Table 5.7: Trigger efficiencies calculated using signal samples. Different cuts are used in the analysis and their relative gain is shown. `1`μ represents single muon trigger, `1`μ`+3Jets` represents the combination of single muon plus three jets trigger while `1`μ`||1`μ`+3Jets` represents the logical "OR" between the single muon trigger and single muon plus three jets trigger.

Trigger Efficiencies				
Cuts	**1μ**	**1μ+3Jets**	**1μ||1μ+3Jets**	**Relative Gain(%)**
Presel	0.512±0.008	0.340±0.008	0.617±0.008	19
Njets ≥2	0.509±0.008	0.347±0.008	0.615±0.008	19
NLightJets≥2	0.50±0.01	0.43±0.01	0.63±0.01	23
NbJets≥2	0.48±0.01	0.35±0.01	0.65±0.01	35
E^t_{miss}	0.49±0.01	0.47±0.01	0.65±0.01	32
P_t^{WW}	0.55±0.07	0.49±0.07	0.591±0.004	93
P_t^{bb}	0.60±0.01	0.58±0.01	0.66±0.06	90
m_{bb}	0.37±0.07	0.35±0.08	0.53±0.08	43

Table 5.8: Trigger efficiencies calculated using signal samples. Different cuts are used in the analysis and their relative gain is shown. `1e` represents single electron trigger, `1e+3Jets` represents the combination of single electron plus three jets trigger while `1e||1e+3Jets` represents the logical "OR" between the single electron trigger and single electron plus three jets trigger.

Trigger Efficiencies				
Cuts	**1e**	**1e+3Jets**	**1e||1e+3Jets**	**Relative Gain(%)**
Presel	0.522±0.008	0.330±0.008	0.653±0.008	25
Njets ≥2	0.489±0.008	0.347±0.008	0.620±0.008	29
NLightJets≥2	0.52±0.01	0.43±0.01	0.65±0.01	25
NbJets≥2	0.47±0.01	0.39±0.01	0.68±0.02	44
E^t_{miss}	0.49±0.01	0.47±0.01	0.65±0.01	32
P_t^{WW}	0.39±0.07	0.30±0.07	0.451±0.003	15
P_t^{bb}	0.50±0.01	0.48±0.01	0.66±0.06	37
m_{bb}	0.37±0.07	0.35±0.08	0.53±0.08	43

5.5 1 Lepton + 3 Jets Trigger Scale Factor Computation

To measure the efficiency of lepton plus three jets triggers, only real and reconstructed lepton and jets were used. For lepton plus three jets trigger efficiency one needs to take into account only unprescaled triggers. Prescaled is applied if the rate at which the trigger select the events too large and is difficult to save all acquired events therefore only one or a few out of total number of events (N) is selected by the trigger. N is called "prescaling factor". Unprescaled trigger trigger every event and store them if they fulfill the selection requirements. An unbiased event selection is taken into account to find the trigger efficiency. To calculate the trigger efficiency using the MC samples the event samples must contain an offline reconstructed objects which was used in the trigger decision. Trigger efficiencies can be defines in several ways. For example, an initial sample with N_0 electrons and $N^i_{trigger}$ are the number of electrons that passes the trigger i.e $\epsilon = \frac{N^i{}_{trigger}}{N_0}$.

To measure the trigger efficiency scale factors, one needs a reference process that is abundant in statistics and well known for example $t\bar{t}$. Due to this reason trigger efficiency scale factor in data is measured by subtracting all the backgrounds except the semileptonic $t\bar{t}$ and it is similar to the signal as much as possible as well. The tables 5.3 and 5.4 show that $t\bar{t}$ is dominats over all backgrounds. As per literature review the lepton part of the scale factor is somehow known, due to this reason this thesis is concentrated only on the jet part. This efficiency is computed at the level where b-jets were greater than two in the cutflow. The efficiency as a function of the jet kinematic variables i.e p_T and η can be expressed as:

$$\epsilon_{trigg}(P_T, |\eta|_{Jet}) = \frac{N_{ev}(P_T, |\eta|Jet1) - (1Jet\_Trigg\_Pass)}{N_{ev}(P_T Jet1, |\eta|Jet1)} \tag{5.4}$$

Where N_{ev} is the total number of events.

The total efficiency for one lepton trigger of all the three jets is the product of the jets efficiencies and can be written mathematically as written below for data and MC respectively. This is valid only if the trigger efficiency for each object is uncorrelated.

$$\epsilon^{data}_{trigger} = \epsilon^{data}_{jet1} \times \epsilon^{data}_{jet2} \times \epsilon^{data}_{jet3} \tag{5.5}$$

And for Monte Carlo

$$\epsilon^{MC}_{trigger} = \epsilon^{MC}_{jet1} \times \epsilon^{MC}_{jet2} \times \epsilon^{MC}_{jet3} \tag{5.6}$$

The level of agreement of the measured efficiency, ϵ_{data}, with the efficiency measured with the same

method in simulation, ϵ_{MC}, is expressed as the ratio of these two called efficiency "scale factor" (SF). Events were triggered independently by the single lepton triggers.

$$ScaleFactor = \frac{\left(\frac{1Lep+3Jets}{1Lep}\right)^{data}}{\left(\frac{1Lep+3Jets}{1Lep}\right)^{MC}} \tag{5.7}$$

This quantity describes the deviation of the simulation from the real detector.

The datasets used to compute the trigger efficiency scale factor correspond to an integrated luminosity of $15.2fb^{-1}$ for muon plus three jets trigger (run number 297730−305380) and $10.4fb^{-1}$ for electron plus three jets trigger (run number 297730−311481) recorded in 2016. The reason for the reduced dataset is that the lepton plus three jets triggers were not unprescaled in the 2015 and 2016 data taking. Therefore this study is meant for the development of this type of triggers in the future Run 3 LHC data taking.
In general any distribution as a function of any offline variable is refered as a `turn-on curve` of a specific trigger. The `trurn-on curve` behavious like a step function and is composed of three regions:

1. where the efficiency is flat i.e looks like close to zero;
2. an intermediate region where slope is large; sharp;
3. where the efficiency is flattens out;

The flatnes shows that the efficiency is zero while below the threshold the trigger is fully efficient: having approximately constant efficiency and the efficient region is called plateau and the average efficiency in the plateau region is called plateau efficiency. Incase of jet triggers the plaeau is always close to one because jets are hard to miss if they have enough high energy. The region where the trigger efficiency changes from zero to any higher values is known as `turn-on region`. If the `turn-on region` is wider the `turn-on curve` is slow and if it is very narrow the `turn-on curve` is steep. In Figure 5.5 and 5.6 the lepton plus three jets over single lepton trigger efficiencies is plotted for data and MC together with the ratio of the two, called scale factor for muon and electron channels separately. The trigger efficiency as a function of b-tagged jet P_T starts around 20 GeV, sharply goes up and then saturates around 70 GeV, this region is known as plateau region showing that efficiency is less than one fractionally. The scale factor is less than one in particular at low jet P_T, this means that the MC is overestimating the trigger efficiency and needs to be corrected. The trigger efficiency scale factor and the efficiency of the one lepton plus three jet is almost the same. The trigger efficiency and the scale factor show a weaker dependent from the b-jet η. The scale factor is almost flat while the trigger efficiency of the lepton plus three jets trigger shows a higher

efficiency at the central part. The trigger efficiency and the scale factor is constant as a function of ϕ so there is no need to apply normalisation correction. The trigger efficiency as a function of the light jet P_T, η and ϕ is shown in figure 5.7 and 5.8 for muon and electron respectively. The light jets are those coming from the W decay. The behaviour of these light jet distributions is almost the same, for both the electorn and muon channels, as that of b-tagged jets described above.

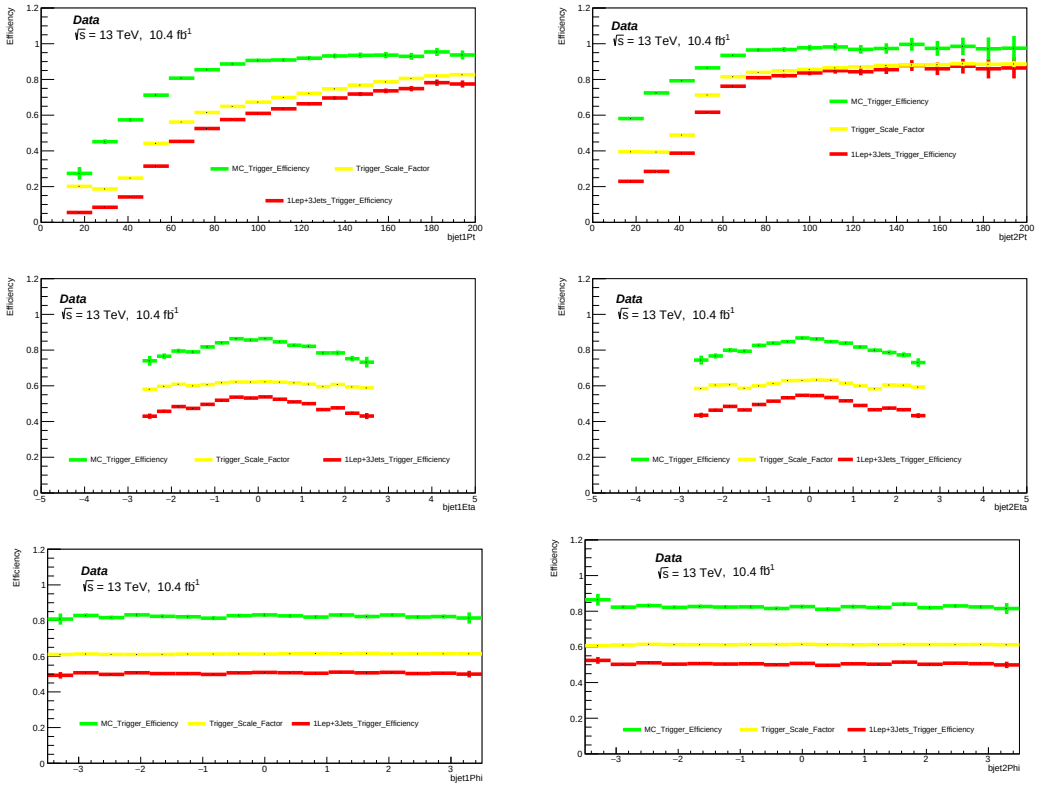

Figure 5.5: **Muon Channel:** The distributions are the turn-on cuves of b-jet1 and b-jet2 plotted P_T, η and ϕ against efficiency.

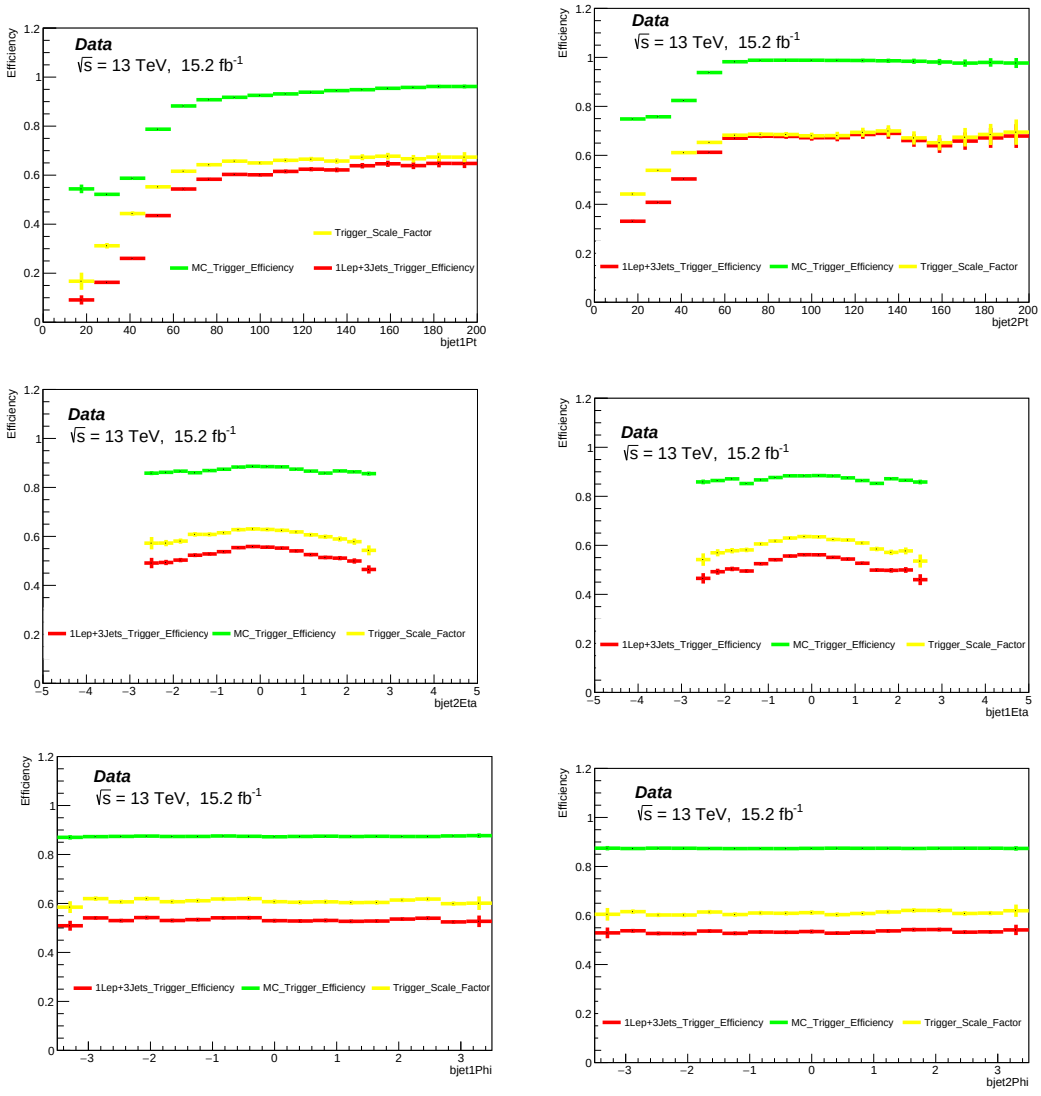

Figure 5.6: **Electron Channel:** The distributions are the turn-on cuves of b-jet1 and b-jet2 plotted P_T, η and ϕ against efficiency.

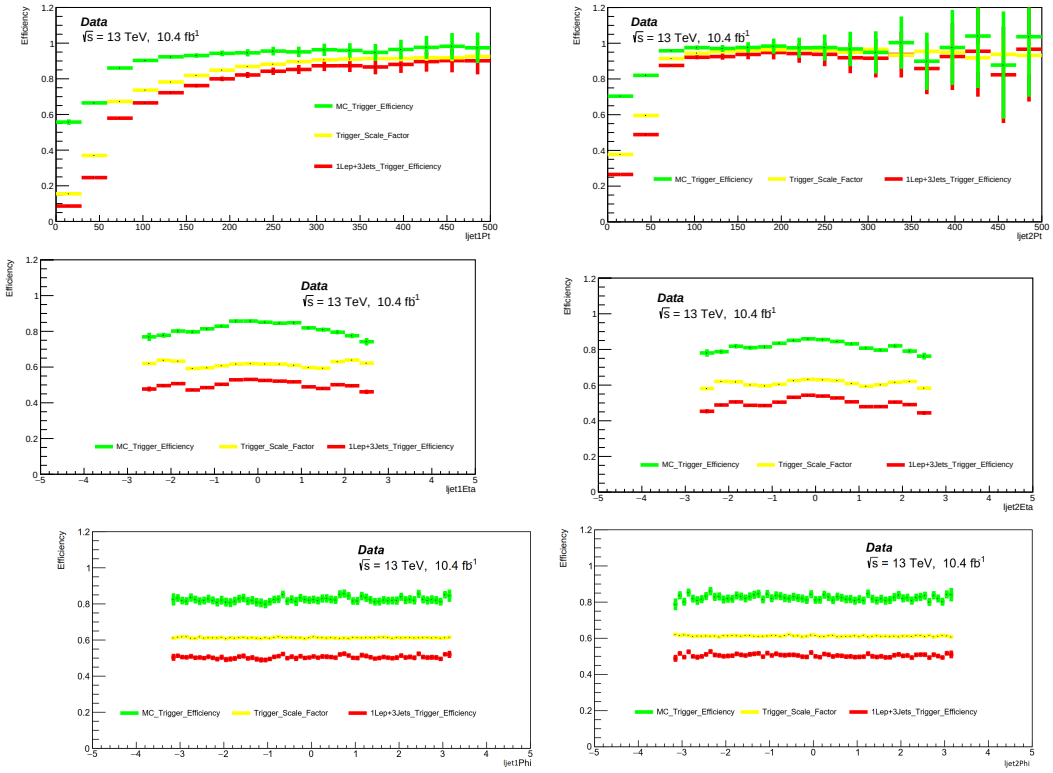

Figure 5.7: **Muon Channel:** The distributions are the turn-on cuves of light jet1 and light jet2 plotted P_T, η and ϕ against efficiency.

5.6 Systematic Uncertainties

This section describes the sources of systematic uncertainties considered in the analysis. These uncertainties are divided into four categories: experimental uncertainties, uncertainties on the data driven background estimation, uncertainties on the modelling of background processes estimated from simulation, theoretical uncertainties on the signal processes. In the statistical analysis each systematic uncertainty is treated as a nuisance parameter the names of which are defined below. These systematic variations are estimated on the final expected yield in the signal regions.

5.6.1 Experimental Uncertainties

Each reconstructed object has several sources of uncertainties, each of which are evaluated separately. Wherever possible, we follow the latest available recommendations from the combined performance (CP) groups. The leading instrumental uncertainties are the uncertainty on the b-tagging efficiency and the jet energy scale (JES).

5.6.2 Luminosity

The uncertainty in the combined 2016 integrated luminosity is 2.1%10. It is derived, following a methodology similar to that detailed in [43], from a preliminary calibration of the luminosity scale using x-y beam-separation scans performed in August 2015 and May 2016. The luminosity uncertainty is applied to those backgrounds estimated from simulation and the signal samples.

5.6.3 Muons Reconstruction Uncertainties

The following systematic uncertainties are applied to muons in estimations based on the simulation:

1. Identification efficiency: The efficiencies are measured with the tag and probe method using the Z mass peak.

2. Energy and Momentum scales: These are also measured with Z mass line shape, and provided by the CP groups.

5.6.4 Trigger Reconstruction Uncertainties

Systematic uncertainties on the efficiency of electron and muon triggers are evaluated as recommended by the corresponding combined performance groups as documented here:

1. Identification efficiency: The efficiencies are measured with the tag and probe method using the Z mass peak.

2. Energy and Momentum scales: These are also measured with Z mass line shape, and provided by the CP groups.

5.6.5 Electron Reconstruction Uncertainties

The following systematic uncertainties are applied to electron in estimations based on the simulation:

1. Identification efficiency: The efficiencies are measured with the tag and probe method using the Z mass peak. They include contributions from reconstruction, identification and isolation;

2. Energy and Momentum scales: These are also measured with Z mass line shape, and provided by the CP groups.

5.6.6 Jet Reconstruction Uncertainties

The jet energy uncertainties are derived based on in situ measurements performed during Run 2 conditions [44]. The jet energy resolution uncertainty is evaluated by smearing jet energies according to the systematic uncertainties of the resolution measurement [45]. The uncertainty in the b-tagging efficiency is evaluated by propagating the systematic uncertainty in the measured tagging efficiency for b-jets [46]. The "Loose" reduction scheme is used.

5.6.7 Missing Transverse Energy

The systematic uncertainties related to the missing transverse energy are obtained by the propagation of the systematic uncertainty on the objects that build the MET, in particular the muon, electron and jets energy resolution and scale.

5.6.8 d_0^{sig} Uncertainties

The uncertainty due to the d_0^{sig} cut has been evaluated by making the ratio between the efficiency of the cut for data and the efficiency of the cut for the MC background samples. We selected di-electron or di-muon event, requiring an invariant di-leptons mass within 80-100 GeV Z Mass window. To be as similar to our signal region as possible but to keep high statistics, loose preselection cuts are applied in selecting the events. The leading lepton is required to have $P_T > 27$ GeV and $Et > 25$ GeV. At least 4 resolved jets are required of which exactly 2 are b jets. The d_0^{sig} distributions for data and MC samples for each lepton channel are shown in the Figure 5.8, in Figure 5.9 the relative ratio of the total distributions is shown. The ratio of the efficiency of the d_0^{sig} cut for data over MC samples si about 96%, this is equivalent if the ratio is estimated by using only muons or only electrons. The difference of this ratio from one is the fractional uncertainty due

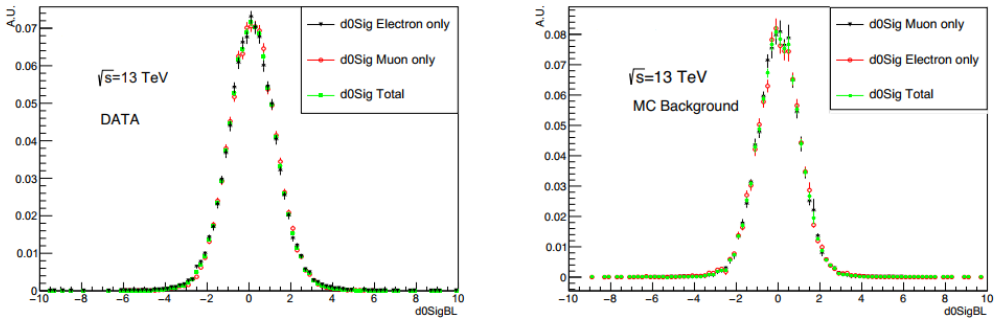

Figure 5.8: d_0^{sig} distributions for data and background MC samples, identifying the lepton channel.

to the d_0^{sig} cut efficiency. This results in about 4% for the d_0^{sig} uncertainty independent from the lepton flavour.

5.7 Background Modelling Uncertainties

The main systematic uncertainties in the background estimate arise from the potential mis-modelling of background components. For $t\bar{t}$ background, MC simulation is used to derive the acceptances in all analysis regions, while the normalisation is taken from the top control region and applied in the signal regions. Therefore, the acceptance ratio between signal and control regions is affected by theoretical uncertainties in the simulated $t\bar{t}$ sample. These uncertainties are estimated by considering five sources: the matrix element generator used for the $t\bar{t}$ simulation and the matching scheme used to match the NLO matrix element with the parton shower, the parton shower modelling, the initial-state (Initial State Radiation, ISR) and final-state (Final State Radiation, FSR) gluon emission modelling, the dependence on the choice of the PDF set and the dependence on the renormalisation and factorisation scales. Matrix element generator and matching systematic uncertainties are computed by comparing samples generated by aMC@NLO [47] and Powheg, both interfaced with Herwig++ for showering and fragmentation. Parton shower systematic uncertainties are computed by comparing samples generated using Powheg+Pythia6 and Powheg+Herwig++. Initial-state and final-state radiation systematic uncertainties are computed by varying the generator parameters from their nominal values to increase or decrease the amount of radiation. The PDF uncertainties are computed using the eignevenctors of the CT10 PDF set. Uncertainties due to missing higher-order corrections, labelled scale uncertainties, are computed by independently scaling the renormalisation and factorisation scales in aMC@NLO+Herwig++ by a factor of two, while keeping the renormalisation/factorisation scaling ratio between 1/2 and 2. These systematic uncertainties are summarised in Table 5.9.

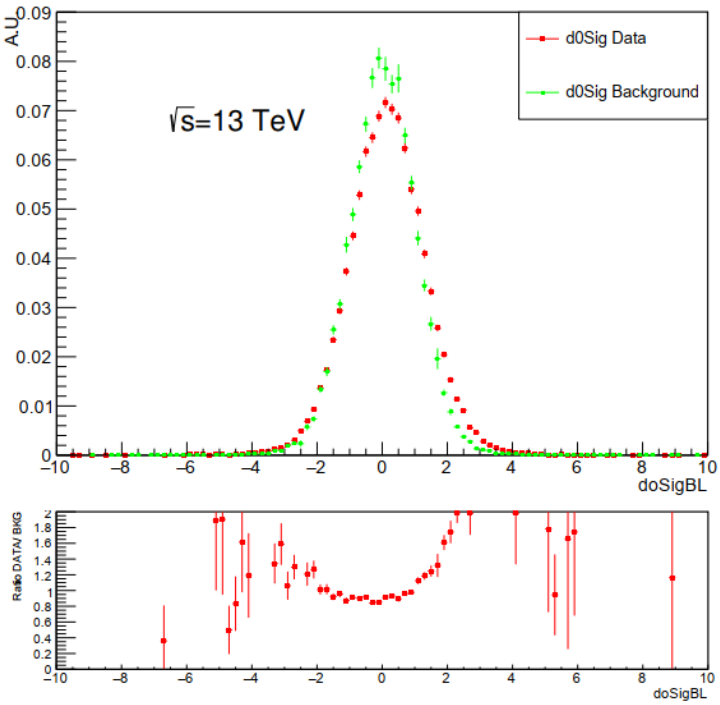

Figure 5.9: d_0^{sig} distributions and the relative ratio for data and background MC samples.

Table 5.9: Percentage uncertainties from $t\bar{t}$ modelling on the $t\bar{t}$ background contributions in all signal regions of the resolved analysis.

Source	Non-res (%)
Matric element	7
Parton shower	4
ISR/DFR	15
PDF	5
Scale	2
Total	18

Uncertainties in the modelling of W+jets background are computed in each signal region (SR) and top control region (CR). Three sources of uncertainty are considered: scale variation, PDF set variation and generator modelling uncertainties. Scale uncertainties are computed by scaling the nominal renormalisation and factorisation scales by a factor of two. PDF uncertainties are computed using the NNPDF [48] error set, while generator modelling uncertainties are obtained by comparing the nominal Sherpagenerated sample with a sample generated with Alpgen [49] and showered with Pythia6 [50]. For the data-driven multijet background, three sources of uncertainty are identified. The non-closure correction term F is computed using data at an early stage of the selection sequence, where contamination by the signal can be considered negligible. Its difference from the value obtained using a simulated multijet event sample is 40% and is assigned as an uncertainty in the multijet estimation. The F value can be affected by the analysis selection requirements. A systematic uncertainty (extrapolation uncertainty) is added by comparing the maximum variation among the F values evaluated after each selection requirement. Finally the uncertainty due to the dependence of the F value on lepton flavour (flavour uncertainty) is computed as the maximum difference between the nominal F value and the F value calculated for electrons and muons separately. The extrapolation (flavour) uncertainty is found to be 16% (9%) for the non-res selection, 32% (9%) for the m500 and low-mass resonant selections, and 45% (6%) for the high-mass resonant selection. Single-top-quark production is one of the smaller backgrounds in this analysis. Theoretical cross-section uncertainties vary from 5% for associated Wt production to 4% for s- and t-channel single-top production. The largest of these is conservatively assigned to all single-top production modes. Further modelling systematic uncertainties are calculated by employing the difference between the nominal sample using the Diagram Removal scheme described in Ref. [51] and a sample using the Diagram Subtraction scheme for the dominant single-top production mode, Wt. The uncertainties are 50%, for the non-res, m500 and low-mass analyses, and 80% for the high-mass analysis. Systematic uncertainties in the signal acceptance are computed by varying the renormalisation and factorisation scales with a variation of up to a factor of two, and using the same procedure as for the $t\bar{t}$ background. PDF uncertainties are computed using PDF4LHC15_30 [52] PDF sets, which include the envelope of three PDF sets, namely CT14, MMHT14, NNPDF3.0.

The resulting uncertainties are less than 1.1% for the scale and less than 1.3% for the PDFs. Parton shower uncertainties are computed by comparing the Herwig++ showering with that of Pythia8, and this results in less than 2% uncertainty. The detector-related systematic uncertainties affect both the background estimate and the signal yield. In this analysis the largest of these uncertainties are related to the jet energy scale (JES), jet energy resolution (JER), b-tagging efficiencies and mis-tagging rates. The JES uncertainties for the small-R jets are derived from $\sqrt{s} = 13$ TeV data and simulations [53], while the JER uncertainties are extrapolated from 8 TeV data using MC simulations [55]. The uncertainty due to b-tagging is evaluated following the procedure described in Ref. [56]. The uncertainties associated with lepton reconstruction and energy measurements have a negligible impact on the final results. All lepton and jet measurement uncertainties are propagated to the calculation of E_T , and additional uncertainties are included in the scale and resolution of the soft term. The overall impact of the E_T soft-term uncertainties is also small. Finally, the uncertainty in the combined integrated luminosity is 3:2% [57]. The systematic contributions in the scaling factor σ_sig for the non-resonant signal and three scalar-signal mass hypotheses, 500 GeV, 1000 GeV and 2000 GeV, in the resolved analysis in the table 5.10.

Table 5.10: Systematic contributions (in percentage) to the total error in the scaling factor σ_sig for the non-resonant signal and three scalar-signal mass hypotheses, 500 GeV, 1000 GeV and 2000 GeV, in the resolved analysis. The first column quotes the source of the systematic uncertainty. The "-" symbol indicates that the specified source is negligible. The contribution is obtained by calculating the difference in quadrature between the total error in σ_sig and that obtained by setting constant the nuisance parameter(s) relative to the contribution(s) under study.

Systematic Source	Resolved Analysis (%)			
	Non-Res (%)	500 GeV	1000 GeV	2000 GeV
$t\bar{t}$ modeling ISR/FSR	+30/-20	+10/-5	+7/-4	+2/-2
Multijet uncertainity	+10/-10	+20/-10	+20/-20	+30/-30
$t\bar{t}$ Matirx Element	+10/-10	-	-	-
W jets modeling PDF	+4/-7	+10/-10	+2/-6	+7/-5
W jets modeling scale	+9/-10	+9/-4	+9/-2	+20/-10
W jets modeling gen.	+10/-8	+10/-10	+9/-1	+9/-9
b-tagging	+30/-20	+11/-5	+7/-6	+30/-30
JES/JER	+13/-20	+20/-20	+50/-50	+10/-6
Pile-up reweighting	+3/-10	+5/-3	+9/-10	+6/-6
Total systematic	+60/-80	+70/-70	+60/-70	+40/-60

5.8 Result

After applying the kinematic selection requirements (described in 5.3), the invariant mass of the HH system m_{HH} distribution are shown in figure 5.10. Within the total uncertainity data and the MC are inagreement. The m_{HH} distributions shown are for the non-resonant and the two graviton hypothesis with $c = 1.0$ and $c = 2.0$. The scalar samples are simulated in the narrow-width approximation, so the reconstructed width is exclusively due to the detector resolution.

The numbers of events in the signal and control regions (the $t\bar{t}$ control region and the C region of the multijet estimation procedure) are simultaneously fit using a maximum-likelihood approach. The fit includes six contributions: signal, W+jets, Z+jets, $t\bar{t}$, single-top-quark production, diboson and multijet. The $t\bar{t}$ and multijet normalisations are free to float, the C region of the ABCD method being directly used in the fit, while the diboson, W+jets and Z+jets backgrounds are constrained to the expected SM cross sections within their uncertainties.

The fit is performed after combining the electron and muon channels. Statistical uncertainties due to the limited sample sizes of the simulated background processes are taken into account in the fit by means of nuisance parameters, which are parameterised by Poisson priors. Systematic uncertainties are taken into account as nuisance parameters with Gaussian constraints. For each source of systematic uncertainty, the correlations across bins and between different kinematic regions, as well as those between signal and background, are taken into account.

No significant excess over the expectation is observed and the results were used to evaluate an upper limit at the 95% confidence level (CL) on the production cross section times the branching fraction for the signal hypotheses under consideration. The exclusion limits were calculated with a modified frequentist method, also known as CLs, and the profile-likelihood test statistic. None of the considered systematic uncertainties is significantly constrained or pulled in the liklihood fit.

In the non-resonant signal hypothesis the observed (expected) upper limit on the $\sigma\ (pp \rightarrow HH) \times B(HH \rightarrow WWbb)$ at 95% CL is :

$$\sigma\ (pp \rightarrow HH) \times B(HH \rightarrow WWbb) < 2.5\ (2.5^{1.0}_{-0.7})\text{pb}$$

The branching fraction $B(HH \rightarrow WWbb) = 2 \times B(H \rightarrow bb) \times B(H \rightarrow WW) = 0.248$ is used to obtain the following observed (expected) limit on the HH production cross section at 95% CL:

$$\sigma\ (pp \rightarrow HH) < 10\ (10^{4}_{-3})\text{pb}$$

which corresponds to 300 (300^{100}_{-80}) times the SM predicted cross section. Including only the statistical uncertainty, the expected upper limit for the non-resonant production is 190 times the SM prediction. This result, when compared with other HH decay channels, is not competitive. This is mainly due to the similarity of the reconstructed m_{HH} spectrum between the non-resonant SM signal and the $t\bar{t}$ background that makes the separation between the two processes difficult.

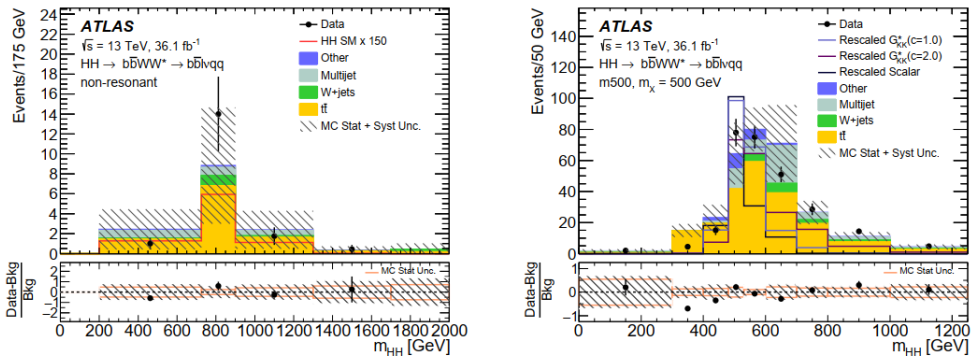

Figure 5.10: m_{HH} distributions for non-resonant and m500 selections in the resolved analysis. For each selection the corresponding signal hypothesis, non-resonant, scalar resonance, and graviton with $c = 1.0$ and $c = 2.0$, is shown. For scalar and graviton signals, resonances with mass 500 GeV are shown. The lower panel shows the fractional difference between data and the total expected background with the corresponding statistical and total uncertainty. The non-resonant signal is multiplied by a factor of 150 with respect to the expected SM cross section. The scalar signal is multiplied by a factor of 5, the graviton $c = 1{:}0$ by a factor of 5 and the graviton $c = 2{:}0$ by a factor of 1 with respect to the expected upper-limit cross section.

5.8.1 Expectation With The New Triggers

This analysis uses 15.2 fb^{-1} and 10.4 fb^{-1} for muon and electron plus three jets triggers of data collected at the center of mass energy $\sqrt{s}$ = 13 TeV and presents a search for Higgs boson pair production where one Higgs boson decays via $h \to b\bar{b}$ and other Higgs boson via $h \to WW^* \to l\nu q\bar{q}$. Trigger efficiency is calculated and is important because the expected signal yield depends on the trigger efficiency, that contributes to the signal acceptance. In the $hh \to WWb\bar{b}$ ATLAS published [58] the limits which were affected mostly by the statistical uncertainty and were less sensitive. The old analysis used single lepton triggers with a threshold of 26 GeV. Due to the low Higgs mass value, the lepton from the W decay has a spectrum that largely populates the low P_T values, therefore the trigger efficiency is low. A new trigger has been deployed that, requiring three jets in addition to the single lepton, allows to enhance the background rejection and reduce the trigger rate, allowing to lower the P_T threshold on the lepton from 26 GeV to 14 GeV allowing 43% signal efficiency are reported in table 5.7 and 5.8. An upper limit is set on the cross section of non-resonant pair production σ ($pp \to HH$) $<$ 10 (10^{4}_{-3})pb at 95% confidence level corresponding to 300 times the predicted SM cross section. Given the result of this work, in order to bring relevant sensitivity improvement to the HH non-resonant SM searches in this channel at the LHC and at future colliders, more advanced analysis techniques, development of new methods for the normalisation of the $t\bar{t}$ background, and a more refined estimation of the multijet background, need to be deployed.

BIBLIOGRAPHY

[1] S. L. Glashow, "partial Symmetries of Weak Interactions," Nucl. Phys., vol. 22,pp. 579-588, 1961. www.sciencedirect.com

[2] S. Weinberg, "A Model of Leptons," Phys. Rev. Lett., vol. 19, pp. 1264-1266, 1967. journals.aps.org

[3] A. Salam, "Weak and Electromagnetic Interactions," Conf. Proc., vol. C680519, pp. 367-377, 1968. link.springer.com

[4] J. Beringer et al., Review of Particle Physics (RPP), Phys.Rev., D86:010001, 2012 inspire.net

[5] Handbook of LHC Higgs Cross Sections: 4. Deciphering the Nature of the Higgs Sector," arXiv:1610.07922 [hep-ph]

[6] "LHC Higgs Cross Section Working Group". https://twiki.cern.ch/twiki/bin/view/LHCPhysics/LHCHXSWG

[7] ATLAS Collaboration, Observation of a new particle in the search for the Standard Model Higgs boson with the ATLAS detector at the LHC, Phys.Lett. B716 (2012) 1-29

[8] CMS Collaboration, Observation of a new boson at a mass of 125 GeV with the CMS experiment at the LHC, Phys.Lett. B716 (2012) 30-61

[9] ATLAS and CMS collaborations, Combined Measurement of the Higgs Boson Mass in pp Collisions at s = 7 and 8 TeV with the ATLAS and CMS Experiments, arXiv:1503.07589v1

[10] F. Englert and R. Brout, "Broken Symmetry and the Mass of Gauge Vector Mesons," 3788 Phys. Rev. Lett. 13 (1964) 321-323

[11] G. S. Guralnik, C. R. Hagen, and T. W. B. Kibble, "Global Conservation Laws and 3792 Massless Particles," Phys. Rev. Lett. 13 (1964) 585-587

[12] P. W. Higgs, "Broken Symmetries and the Masses of Gauge Bosons," Phys. Rev. Lett. 3790 13 (1964) 508-509

[13] Observation of a new particle in the search for the Standard Model Higgs boson with the ATLAS detector at the LHC. https://arxiv.org/abs/1207.7214

[14] O. S. Bruning, P. Collier, P. Lebrun, S. Myers, R. Ostojic, J. Poole, and P. Proudlock, LHC Design Report Vol.1: The LHC Main Ring,.

[15] https://home.cern/about/accelerators/linear-accelerator-2

[16] https://home.cern/about/accelerators/super-proton-synchrotron

[17] M. Bajko et al., Report of the Task Force on the Incident of 19th September 2008 at the LHC. oai:cds.cern.ch:1168025, Tech. Rep. LHC-PROJECT-Report-1168. CERN-LHC-PROJECT-Report-1168, CERN, Geneva, Mar, 2009. https://cdsweb.cern.ch/record/1168025.2.2

[18] ATLAS Collaboration, ATLAS inner detector: Technical Design Report

[19] ATLAS Collaboration, ATLAS inner detector: Technical Design Report, 2. Technical Design Report ATLAS. CERN, Geneva, 1997. https://cdsweb.cern.ch/record/331064.3.1

[20] ATLAS Collaboration, ATLAS muon spectrometer: Technical Design Report. Technical Design Report ATLAS. CERN, Geneva, 1997. https://cdsweb.cern.ch/record/331068.3.1

[21] ATLAS collaboration, Inner Detector: Technical Design Report, 1, CERN-LHCC-97-016; Inner Detector: Technical Design Report, 2, CERN-LHCC-97-017.

[22] A. Ahmad, Z. Albrechtskirchinger, P. Allport, J. Alonso, L. Andricek, et al., The Silicon microstrip sensors of the ATLAS semiconductor tracker, Nucl.Instrum.Meth. A578 (2007) 98-118.

[23] "Web Page: TE-EPC-LPC in LHC." http://te-epc-lpc.web.cern.ch/te-epc-lpc/machines/lhc/general.stm.

[24] Web Page: ATLAS Experiment - Photos." http://www.atlas.ch/photos/index.html.

[25] J. D. Long, Observation and Measurements of the Higgs Boson with the $H \to WW \to ll\nu\nu$ Decay, CERN-THESIS-2015-046. Cited at pages 23, 125.

[26] ATLAS Collaboration, The ATLAS Experiment at the CERN Large Hadron Collider, Journal of Instrumentation 3 (2008), no. 08 S08003. Cited at pages 21,25, 26, 29, 31, 32.

[27] Kerstin Hoepfner, Particle Detectors: Muon Detectors, May, 2016, `https://indico.cern.ch/event/526767/`, CERN Academic Trainign Lecture Regular Programme.

[28] ATLAS Collaboration, Commissioning of the ATLAS Muon Spectrometer with cosmic rays, `Eur.Phys.J.C70(2010)875`, `arXiv:1006.4384[hep-ex]`.

[29] ATLAS Collaboration, The ATLAS Experiment at the CERN Large Hadron Collider, JINST 3 (2008) S08003

[30] ATLAS muon spectrometer: Technical Design Report ATLAS, Geneva: CERN, 1997.

[31] ATLAS Collaboration, The ATLAS Experiment at the CERN Large Hadron Collider, inspire.net.

[32] The ATLAS trigger system: Past, Present and Future. www.sciencedirect.com

[33] ATLAS Collaboration, ATLAS muon spectrometer: Technical Design Report. CERN, Geneva, 1997.

[34] Lenzi, B., R. Nicolaidou, and S. Hassani. "TrackInCaloTools: A package for measuring muon energy loss and calorimetric isolation in ATLAS. Journal of Physics: Conference Series. Vol. 219. No. 3. IOP Publishing, 2010.

[35] Barton, Adam Edward, et al. "Muon reconstruction performance of the ATLAS detector in protonâĂŞproton collision data a $\sqrt{s} = 13$ TeV." European Physical Journal C: Particles and Fields 76.5 (2016).

[36] `https://twiki.cern.ch/twiki/bin/view/AtlasProtected/MuonPerformance#AnchorReconstruction`

[37] ATLAS Collaboration, "Performance of missing transverse momentum reconstruction for the ATLAS detector in the first proton-proton collisions at $\sqrt{s} = 13$ TeV." ATL-PHYS-PUB-2015-027, Jul 2015.

[38] https://arxiv.org/abs/1307.8361

[39] M. Bahr et al., Herwig++ Physics and Manual, Eur.Phys.J. C58 (2008) p. 639, arXiv: 0803.0883 [hep-ph]

[40] N. Kidonakis, Next-to-next-to-leading-order collinear and soft gluon corrections for t-channel single top quark production, Phys. Rev. D83 (2011) 091503, arXiv: 1103.2792 [hep-ph]

[41] T. Gleisberg et al., Event generation with SHERPA 1.1, JHEP 0902 (2009) 007, arXiv: 0811.4622 [hep-ph]

[42] ATLAS Collaboration, The performance of the jet trigger for the ATLAS detector during 2011 data taking, Eur. Phys. J. C 76 (2016) 526.

[43] ATLAS Collaboration, Luminosity Determination in pp Collisions at $\sqrt{s} = 8$ TeV using the ATLAS Detector at the LHC, ATLAS-CONF-2011-116 C 76 (2016) 653, Eur. Phys. J

[44] ATLAS Collaboration, âĂŸJet Calibration and Systematic Uncertainties for Jets Reconstructed in the ATLAS Detector at $\sqrt{s} = 13$ TeVâĂŹ, tech. rep. ATL-PHYS-PUB-2015-015, CERN, 2015

[45] ATLAS Collaboration, Jet energy measurement and its systematic uncertainty in proton-proton collisions at $\sqrt{s} = 7$ TeV with the ATLAS detector, Eur. Phys. J. C75 (2015) 17

[46] ATLAS Collaboration, âĂŸCalibration of b-tagging using dileptonic top pair events in a combinatorial likelihood approach with the ATLAS experimentâĂŹ, tech. rep. ATLAS-CONF-2014-004, CERN, 2014

[47] J. Alwall et al., The automated computation of tree-level and next-to-leading order differential cross sections, and their matching to parton shower simulations, JHEP 07 (2014) 79

[48] R. D. Ball et al., Parton distributions for the LHC Run II, JHEP 04 (2015) 040

[49] M. L. Mangano et al., ALPGEN, a generator for hard multiparton processes in hadronic collisions, JHEP 07 (2003) 001

[50] T. Sjostrand, S. Mrenna, and P. Z. Skands, PYTHIA 6.4 Physics and Manual, JHEP 05 (2006) 026

[51] S. Frixione et al., Single-top hadroproduction in association with a W boson, JHEP 07 (2008) 029

[52] J. Butterworth et al., PDF4LHC recommendations for LHC Run II, J. Phys. G 43 (2016) 023001

[53] ATLAS Collaboration, Jet energy scale measurements and their systematic uncertainties in proton-proton collisions at $\sqrt{s}$ = 13 TeV with the ATLAS detector, Phys. Rev. D 96 (2017) 072002

[54] ATLAS Collaboration, Jet Calibration and Systematic Uncertainties for Jets Reconstructed in the ATLAS Detector at $\sqrt{s}$ = 13 TeV, ATL-PHYS-PUB-2015-015, 2015

[55] ATLAS Collaboration, Measurements of b-jet tagging efficiency with the ATLAS detector using tt events at $\sqrt{s}$ = 13 TeV, JHEP 08 (2018) 089

[56] ATLAS Collaboration, Measurements of b-jet tagging efficiency with the ATLAS detector using tt events at $\sqrt{s}$ = 13 TeV, JHEP 08 (2018) 089

[57] ATLAS Collaboration, Luminosity determination in pp collisions at $\sqrt{s}$ = 8 TeV using the ATLAS detector at the LHC, Eur. Phys. J. C 76 (2016) 653

[58] ATLAS Collaboration, Search for Higgs boson pair production in the $b\bar{b}WW^*$ decay mode at $\sqrt{s} = 13$ TeV with the ATLAS detector arXiv:1811.04671